Gas Migration and Slope Instability in the Danube Fan: Insights from integrated OBS-MCS Seismic Analysis

Helene-Sophie Hilbert[1], Anke Dannowski[1], Jörg Bialas[1], Felix Gross[2,3], Jasper Hoffmann[1,4], Dirk Kläschen[1], Christian Berndt[1]

5 [1] GEOMAR Helmholtz Centre for Ocean Research Kiel, RD Marine Geodynamics, Kiel, Germany
[2] Christian-Albrechts-University Kiel, Institute of Geosciences, Kiel, Germany
[3] Christian-Albrechts-University Kiel, Centre for Ocean and Society, Kiel, Germany
[4] Alfred-Wegener-Institute, Helmholtz Centre for Polar and Marine Research Sylt, Department Coastal Ecology, List, Germany

10 *Correspondence to*: Helene-Sophie Hilbert (hhilbert@geomar.de)

Key Points:

- Underconsolidated, clay-rich sediments in the Danube Fan generate mechanically weak layers that are prone to slope failure, especially when disturbed by gas pressure build-up or external forces.
- Gas hydrates are present but with low concentrations and patchy distribution; free gas accumulates beneath hydrate 15 zones in sandy layers, sealed by impermeable clays.
- The Danube Fan represents a hydrate-poor system, dominated by microbial gas, offering insights into gas hydrate dynamics in fine-grained, deltaic deep-sea environments.

Abstract. Gas hydrates and deltaic deep-sea fans are main features in continental margin systems, influencing slope stability, fluid migration, and carbon cycling. In the northwestern Black Sea, the Danube Fan remains poorly constrained with respect 20 to subsurface structure, sediment strength, and hydrate dynamics. Here, we present high-resolution multichannel seismic (MCS) and ocean-bottom seismometer (OBS) data to characterise sedimentary structure and fluid-related features. Two integrated OBS–MCS profiles reveal underconsolidated, clay-rich levee deposits interspersed with mass-transport units, chaotic facies, and gas-related anomalies. Derived P- and S-wave velocity models indicate low shear strength and high Vp/Vs-ratios in shallow units, consistent with soft, water-saturated sediments. Deeper layers display compaction-driven velocity 25 increases but remain mechanically weak, rendering the slope prone to failure. Our findings suggest that vertical gas migration is widespread, expressed by seismic chimneys, polarity reversals, and velocity pull-downs, with free gas confined below bottom simulating reflectors and in stratigraphic traps. Hydrates likely occur as sparse, patchy pore-filling accumulations, and the lack of S-wave velocity anomalies suggests they do not act as cementing phases, implying little direct influence on sediment strength or slope stability. The hydrate system appears hydrate-poor, possibly reflecting post-glacial re-equilibration. Overall, 30 lithology, gas migration pathways, and high sedimentation rates emerge as primary controls on hydrate formation and slope instability in the Danube Fan.

Plain Language Summary. This study investigates gas hydrate distribution in the Danube Fan, NW Black Sea. Using seismic data and drilling results, we analysed the structure, composition, and gas content of underconsolidated sediments. Gas hydrates are present in low concentration and patchy distribution. Free gas is trapped beneath the hydrate stability zone. The area shows
35   signs of past slope failures linked to weak sediments and gas accumulation. The study provides insights into how gas hydrate systems evolve.

40

1 Introduction

Submarine slope stability and gas hydrate systems are critical components of marine geohazards and carbon cycling along continental margins. In regions such as the Danube Fan, located on the northwestern Black Sea margin, rapid sedimentation,
45   overpressure development, and complex fluid migration contribute to slope instabilities and localised gas accumulations (Popescu et al., 2006, 2004). Understanding these processes is essential not only for assessing landslide risks but also for improving our knowledge of subsurface gas dynamics, which has important implications for marine resource management, carbon storage, and climate change feedbacks.

Gas hydrates, ice-like crystalline compounds of water and gas, typically methane, are stable under high-pressure and low-
50   temperature conditions in marine sediments (Sloan and Koh, 2008). Their stability is sensitive to environmental changes, such as warming bottom waters or sea-level fluctuations, which may trigger dissociation and migration of free gas in the sediment and into the water column (Ruppel and Kessler, 2017). These dynamics are particularly relevant in continental margin settings like the Danube Fan, where gas migration pathways, overpressured sediments, and stratigraphic traps generate favourable conditions for both gas hydrate formation and slope failure (Riedel et al., 2021a; Bialas et al., 2020a; Hillman et al., 2018;
55   Zander et al., 2018).

Combined P- and S-wave analysis, provides a valuable tool for characterising sediment properties and further allow the estimation of V_p/V_s-ratios that allow the identification of lithological changes, detect free gas and gas hydrates in the subsurface. Together with high-resolution multichannel seismic (MCS) imaging and ground-truth data, fluid dynamics can be studied intensively.

60   This study presents two high-resolution seismic profiles across a slump scar in the Danube Fan to investigate the subsurface architecture, sediment consolidation state, and gas hydrate occurrence. By integrating velocity modelling with stratigraphic interpretation and drilling data (MeBo200), we aim to constrain the mechanical and fluid-related processes governing slope failure.

Beyond addressing geohazards, this study has the potential to significantly advance our understanding of fluid migration and
65   gas accumulation in underconsolidated marine sediments. Our insights are crucial for optimising site selection and enhancing monitoring strategies in subsurface projects involving fluid-injection, leakage control, and long-term storage, particularly in high-stakes applications, such as carbon capture and storage (CCS). The observed gas trapping and migration mechanisms are to a certain degree analogous to those required for long-term CO_2 storage in marine settings (e.g., Yip et al., 2013).

2 Geological Setting

70   The Danube Fan is a fine-grained turbidite system on a particularly wide shelf (~120 km) of the northwestern Black Sea. It developed over the past ~900 ka through a succession of stacked channel-levee systems interbedded with mass-transport deposits (MTDs) (Wong et al., 1997; Winguth et al., 2000; Popescu et al., 2001). The fan system extends from the shelf edge at ~100 m water depth to the abyssal plain, where water depths exceed 2200 m (Wong et al., 1997).

Erosional processes dominate the upper slope, primarily within the channel-levee systems, while depositional and
75   aggradational processes prevail along the middle and lower slopes (Popescu et al., 2001). Bathymetric data reveal the presence of several submarine canyons and associated channels, with a predominant NW-SE orientation (Fig. 1).

For consistency with previous studies, we adopt the canyon nomenclature established by Wong et al. (1997) and Winguth, (1998), where the prefix "S" refers to the southern Danube Fan complex. Canyon numbers ascend from the oldest to the youngest, corresponding to successive activity phases and sedimentary sequences. These canyons represent the most recent
80   depositional phase of the Danube Fan, which developed between ~75 ka to 22 ka ago, during the sea-level lowstand associated with the Last Glacial Maximum (LGM; Late Pleistocene Neoeuxinian Stage) (Winguth et al., 2000; Lericolais et al., 2013). During this period, sea-level was ~100-150 m lower than present, resulting in an isolation of the Black Sea from the global oceans (Ryan et al., 1997; Lericolais et al., 2009).

Several studies suggest, that only one canyon was active during each sea level low-stand, with the Viteaz canyon (S5)
85   representing the recently active system (Wong et al., 1997; Winguth et al., 2000; Popescu et al., 2001, 2004). During active
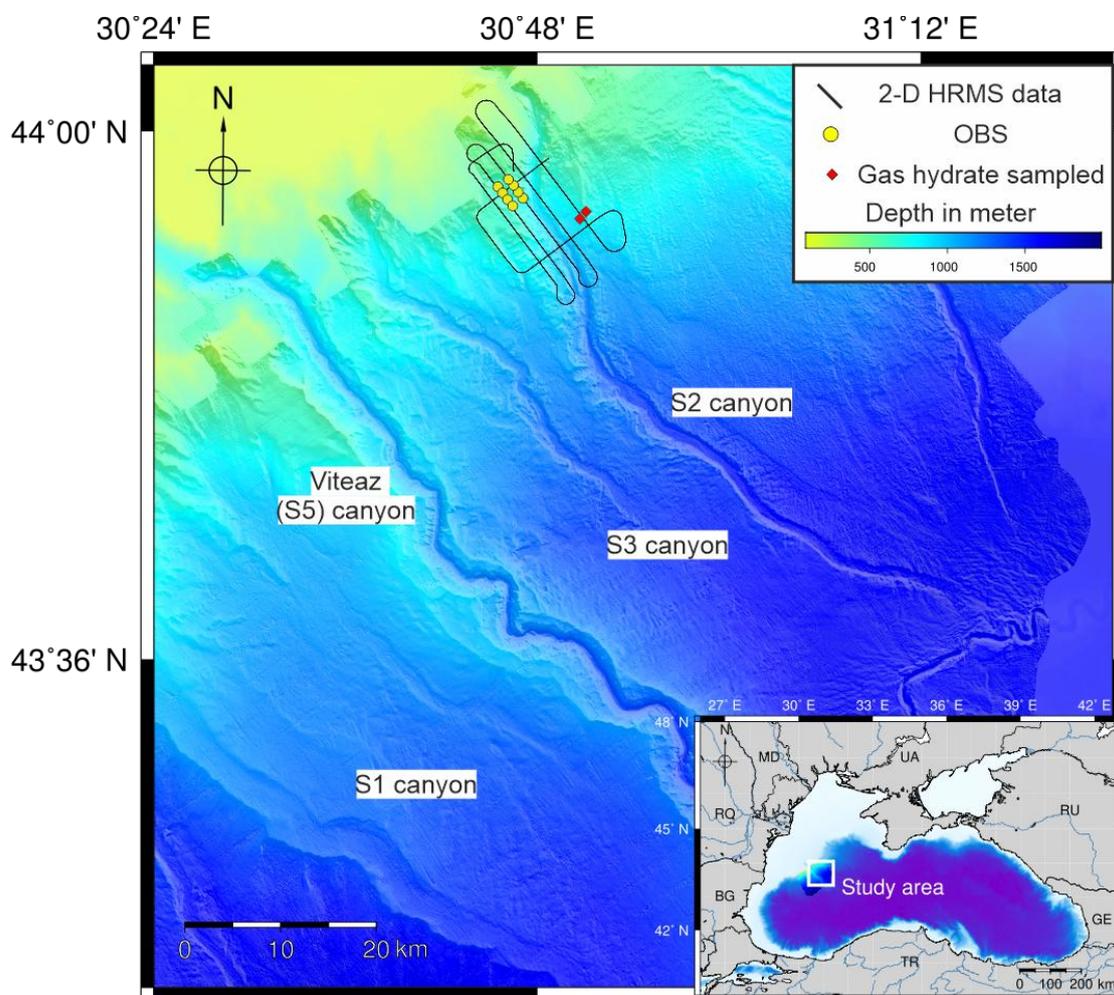
Fig. 1: Bathymetric overview of the Danube deep-sea fan complex, acquired during MSM-34 (Wintersteller & Bialas, 2016) showing the location of the seismic datasets collected on the western flank of the S2 canyon. Red diamonds indicate sites where gas hydrates were sampled during GHASS (Gas Hydrates, fluid Activities and Sediment deformations in the western Black Sea) cruise (Ker & Riboulot, 2015). Inset: Location of the study area in the north-western Black Sea (ETOPO-1; Amante & Eakins, 2009). Country abbreviations: BG = Bulgaria, RO = Romania, MD = Moldavia, UA = Ukraine, RU = Russia, GE = Georgia, TR = Turkey.

phases, the canyons were directly connected to the Danube River and transported large volumes of sediment via channelised turbidity currents towards the deep sea (Popescu et al., 2001). Compared to the more distinctive S5 canyon, S2 exhibits lower sinuosity (Fig. 1). The surrounding seafloor contains extensive MTDs, levee deposits, and fine-grained overbank sediments, including channel overflows (Wong et al., 1997; Badhani, 2016). The isolation of the Black Sea during the LGM and the associated fan sedimentation ceased with postglacial sea-level rise and global reconnection at the end of the Quaternary glaciation, approximately 7500 years ago (Lericolais et al., 2009). Hydrological conditions in the Black Sea have fluctuated in response to glacio-eustatic sea-level changes, alternating between low salinity, oxygenated lacustrine environments and strongly stratified, anoxic marine conditions in deeper waters (Deuser, 1974; Özsoy and Ünlüata, 1997). The onset of deep-

4

water anoxia is closely linked to the formation of sapropels, which result from enhanced biogenic productivity during

95 transitions from limnic to marine settings (Popescu et al., 2007). Today the Black Sea is the world's largest anoxic basin, providing favourable conditions for hydrocarbon formation (Vassilev and Dimitrov, 2002; Jørgensen et al., 2004).

The estimated upper limit of the GHSZ, assuming an average bottom-water temperature of 9 °C (Ross and Degens, 1974), lies at ~720 m water depth (Zander et al., 2017; Riedel et al., 2020), though this depth also depends on the pore water salinity. Pore water salinity in the Black Sea ranges from 22.3 practical salinity units (psu) under marine conditions (Özsoy and Ünlüata,

100 1997) to as low as 3 psu in limnic conditions (Svitoch et al., 2000).

Within the study area, gas flares are observed at water depths shallower than 655 m, the upper limit of the GHSZ (Hillman et al., 2018). Gas samples from the Danube Fan show a primarily biogenic origin, with concentrations up to 99 % methane, indicating in-situ formation (Vassilev and Dimitrov, 2002).

3 Data Acquisition, Processing and Modelling

105 As a part of the multidisciplinary research project SUGAR (**Su**bmarine **Ga**s Hydrate **R**eservoirs) and MIDAS (**M**anaging **I**mpacts of **D**eep-Se**a** Re**s**ource Exploitation), the German research cruise MSM-34 acquired 2-D multichannel seismic (MCS) and 4-component ocean-bottom-seismometer (OBS) data (Dannowski and Bialas, 2025), along with multibeam bathymetry (Bialas et al., 2014). Bathymetric data were collected continuously throughout the cruise using a hull-mounted EM 122 echosounder operating at 12 kHz. The data were processed onboard using MB-systems® (Caress et al., 2008), with sound

110 velocity corrections from regular profiles, manual artefact removal and cleaning, resulting in a gridded dataset with a spatial resolution of 25 x 25 m.

Seismic data acquisition employed a 45 in³/45 in³ Generator-Injector (GI) airgun, towed at 2 m depth and fired at 3 s intervals. At an average vessel speed of ~3.5 kn, this configuration yielded a shot spacing of ~5.4 m. The GI airgun had a centre frequency of ~130 Hz.

115 **3.1 OBS Data and Processing**

Two OBS profiles, designated A and B, were acquired on the western flank of the S2 canyon within the Danube Fan. Each line included four OBS deployments (Fig. 2). The instruments were equipped with 3-component 4.5 Hz geophones and hydrophones, and data were recorded continuously using a Marine Broadband Seismic recorder (Bialas & Flueh, 1999) at a sampling rate of 1000 Hz.

120 OBS data processing included the following steps: (1) clock drift correction, (2) instrument relocation on the seafloor using direct wave arrivals, (3) rotation of the horizontal components into radial and transverse components for each shot (Maercklin, 2001), (4) amplitude balancing (max/min normalisation), and (5) bandpass or low-pass filtering to enhance phase identification during traveltime picking.

Overall, the OBS data quality was high. Multiple P-wave (hydrophone) and converted S-wave (geophone) reflections were

125 clearly identified (Fig. 3). In general, S-wave reflections exhibited a higher signal-to-noise ratio than P-wave signals and were less affected by water-column multiples due to the different frequencies analysed (Fig. 4). To suppress high-frequency noise and emphasise the stable, low-frequency signal content, a bandpass filter of 20-40 Hz for P-waves and a lowpass of 20 Hz for S-waves was applied. Several stations drifted when they were deployed and are now about 30 m offline.

One station (OBS 3002) was excluded from S-wave analysis due to insufficient seafloor coupling. The absence of clear

130 refracted phases across the array restricts the velocity analysis to a localised zone directly underneath each instrument.
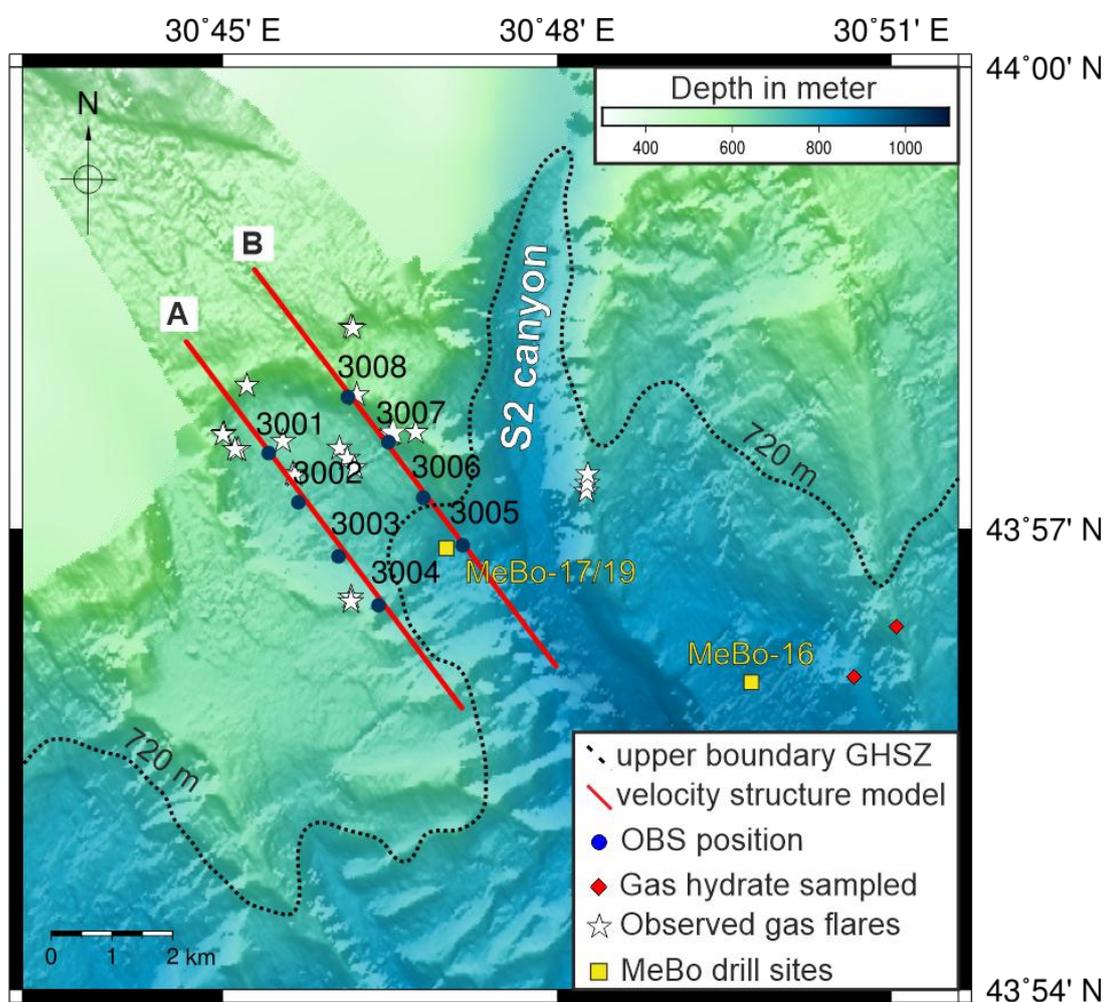

Fig. 2: Detailed bathymetric map of the study area on the western flank of the S2 canyon, gridded at 25 x 25 m resolution. Data gaps were filled with the global ETOPO-1 dataset (1 arc-minute resolution; Amante & Eakins, 2009). The map shows the spatial extent of the velocity models and associated 2-D MCS profiles (red lines), ocean-bottom-seismometer (OBS) positions (blue dots), gas flares observed in the water column (white stars; Hillman et al., 2018), sampled gas hydrates (red diamonds; Ker & Riboulot, 2015), and MeBo200 drilling sites (yellow rectangles; Riedel et al., 2020). The dashed black line indicates the 720 m isobath, representing the estimated upper boundary of the GHSZ (Zander et al., 2017; Riedel et al., 2020).
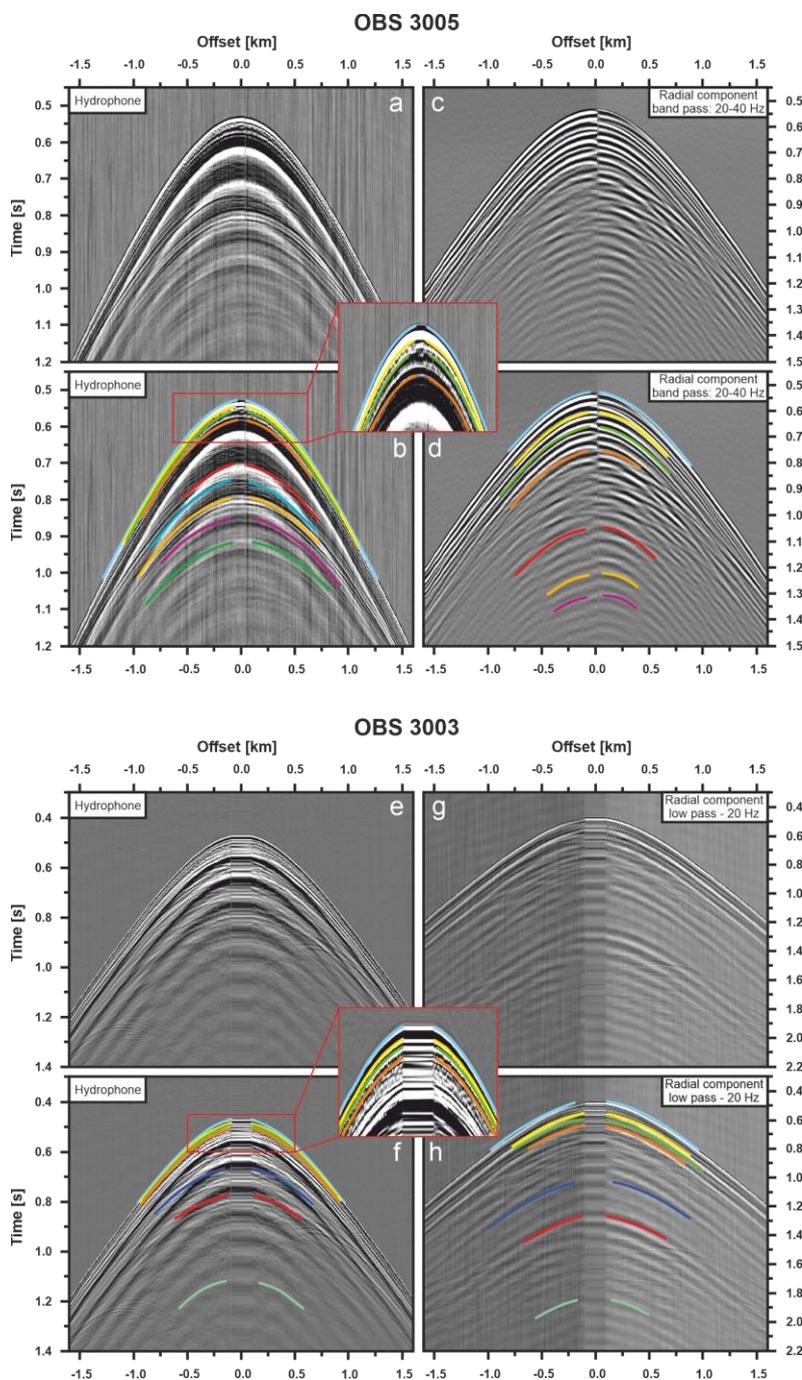
Fig. 3: (a) Hydrophone component of OBS 3005 and (b) identified P-wave phases used for forward modelling. Inset: Enlarged view of near-seafloor P-wave arrivals. (c) Radial component of OBS 3005 and (d) corresponding converted S-wave phases used in forward modelling. (e) Hydrophone component of OBS 3003 and (f) identified P-wave phases. Note that the horizontally stretched onsets around x=0 km result from a lateral offline position of OBS 3003. Inset: Enlarged view of near-seafloor P-wave arrivals. (g) Radial component of OBS 3003 and (h) corresponding converted S-wave phases used for forward modelling. Note that the S-wave panels are shown on a different timescale due to slower wave propagation velocities.
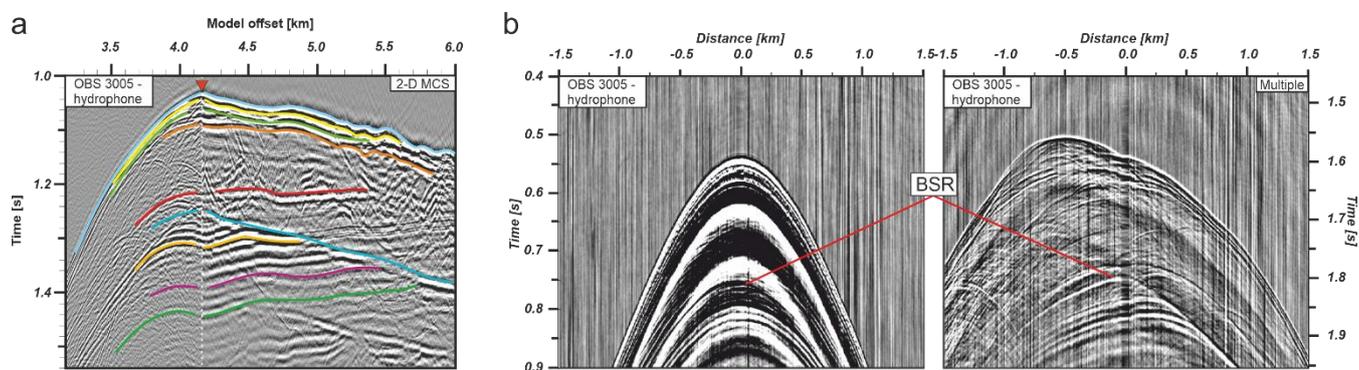
Fig. 4: OBS 3005 hydrophone dataset (a) Alignment of the hydrophone with the 2-D high-resolution MCS data after applying a Butterworth bandpass filter (20-40 Hz) and equal amplitude scaling. The hydrophone data are adapted to the MCS section in terms of onset and offset timing. The MCS time axis is converted into one-way traveltime. (b) BSR identified in the first arrival (left) and corresponding first multiple (right). The BSR is observed as a distinct reflection with reversed polarity relative to the seafloor reflection, consistent with a velocity decrease below the reflector.

3.2 2-D High-resolution MCS Data and Processing

Multichannel seismic (MCS) data were acquired simultaneously with the OBS deployments along profiles A and B (Fig. 2), using a 144-channel streamer. The streamer configuration included a 25 m vibration isolation section, a 55 m tow cable, and 19 active sections of 12.5 m each, yielding a total active length of 237.5 m. Each active section contained 8 channels, with a hydrophone group spacing of 1.5625 m. Data were recorded at a sampling rate of 1000 Hz and binned with a common depth point (CDP) spacing of 1.5625 m.

The MCS data processing workflow comprised the following steps: (1) navigation correction for both streamer and shot positions, (2) crooked-line common mid-point (CMP) binning, (3) gain correction, (4) attenuation of anomalous amplitudes, (5) radon filtering, (6) CMP stacking using water velocity, necessitated by the short streamer length, (7) deconvolution with a prediction lag of 60 ms, averaged over 1000 traces, to suppress injector bubble effects, (8) water-velocity Stolt migration, followed by residual finite-difference migration using spatially and temporally varying velocities from regional profiles (Hillman et al., 2018). Final depth conversion was performed in IHS Kingdom® software, utilising the velocity models derived from the OBS data.

3.3 Phase Identification and OBS-MCS Correlation

The OBS records show both compressional (P-) and shear (S-) wave phases. Phase identification began with picking the P-wave reflections, which were then assigned to specific layers within the seismic velocity model for each station. Prominent reflectors observed in the MCS data served as reference horizons and were cross-checked against corresponding phases in the OBS records. Therefore, the OBS data were aligned to the MCS at zero offset and time-shifted so that the direct water arrivals matched the seafloor reflection in the MCS data, compensating for the two-way traveltime (Fig. 4a). This alignment allowed consistent phase identification across all OBS stations. Additionally, first water multiples were used to help discriminate

overlapping arrivals to identify reflection polarity more clearly, especially where direct arrivals were masked by source-related noise (Fig. 4b). P-wave reflections were typically traceable to source-receiver offsets of up to ~1.2 km (Fig. 3).

Once P-wave arrivals were identified, converted S-wave phases, recorded on the radial components (Fig. 3c and 3g), were

155   assigned to the same reflectors within the velocity model. This step was the most critical in the analysis, relying on joint forward modelling of both P- and S-wave arrivals. Following Digranes et al. (1998), the conversion from P- to S-waves is assumed to occur at the reflector itself. Due to their lower velocities, S-wave reflections could only be traced over shorter offsets, with a maximum source-receiver distance of ~0.9 km (Fig. 3), resulting in a smaller spatial coverage compared to the P-wave data.

160   **3.4 Forward Modelling**

Seismic phases were picked using PASTEUP (Fujie et al., 2008), a graphical user interface (GUI) for Seismic Unix (Stockwell, 1999). Forward modelling was performed with RAYINVR (Zelt and Smith, 1992) using the companion GUI MODELING (Fujie et al., 2008). The initial P-wave velocity structure was adapted from Hillman et al., (2018) and iteratively refined using a trial-and-error forward modelling approach. Interface geometries were locally adjusted by up to ±5 m over ~200 m of profile

165   length in the upper sections and by ±10 m over ~500 m in deeper sections, particularly where OBS instruments were located offline.

RAYINVR computes traveltimes through user-defined velocity and depth grids using a 2-D ray-tracing and forward modelling algorithm (Zelt and Smith, 1992). This process yielded detailed final models extending to ~1.2 km depth, well below the BSR. Subsequently, the velocity structure and layer geometry were jointly refined for both P- and S-waves by modifying the Vp/Vs-

170   ratios within each layer. The plausibility of the P-S-phase correlations was evaluated by examining the S-wave residuals for systematic misfits or unrealistic Vp/Vs-ratio values.

4 Results

4.1 Subsurface Structure of Profile A

Profile A traverses the central part of a slope failure zone to west of the S2 canyon. OBSs 3001 to 3003 are located within the

175   slump scar (Fig. 2), which has an average dip angle of 2.5°. The northwestern headwall forms a prominent ~100 m high step in the seafloor (Fig. 5a), while OBS 3004 is situated near the southwestern scarp of the failure area (Fig. 2). The profile terminates southeast within the levee deposits of the Danube Fan.

Based on traveltime picking and final modelling, the subsurface is divided into three units (Fig. 5). The units comprise of ten model layers (A1-A10), with A1 representing the water column (more details regarding the layers in Supplement S1).

180

Unit 1: Unit 1 comprises the shallowest sediments and is characterised by continuous, high-amplitude reflections. These extend upslope within the slump scar (1.0-5.5 km along profile) and also appear southeast of OBS 3004, with an approximate thickness

of 40-70 m (Fig. 5). Although amplitude strength slightly diminishes in the southeast, intact stratification is maintained across the unit.

185 Northwest of the headwall, a similar reflection pattern is observed just beneath the seafloor. However, due to the modelled pinch-out of layers (A2-A5), the equivalent reflections in this region are incorporated into layer beneath (A8). At the headwall crest, the unit thickens to ~80 m, with less pronounced reflection amplitudes. A distinctive, lenticular structure (M1) about 20 m thick and 500 m wide is embedded within Unit 1, between 1.6-2.0 km model offset, southeast of OBS 3001 (Fig. 5a). This feature displays semi-transparent, sub-parallel internal reflections.

190 **Unit 2:** This unit consists of chaotic seismic facies (CSF) dominated by patchy high amplitudes (Fig, 5a), extending from the toe of the headwall (~0.9 km) to southeast of OBS 3003 (~3.6 km) with a relatively uniform thickness of ~150 m. A prominent downward-dipping reflection (DDR), maintaining the same polarity as the seafloor, terminates the CSF below (Fig. 5a). Above the DDR, the seismic section displays southeast-tilted reflections down to ~800 m depth. Reflections northwest of OBS 3004 (3.5-3.8 km) dip toward the S2 canyon, mirroring the stratification observed northwest of the headwall (F1) for the

195 uppermost 200 m (Fig. 5a). At ~4.4 km model offset and ~700 m depth, localised high amplitudes are present, underlain by chaotic, broken reflections between 800-1000 m depth. A velocity pull-down effect, interpreted as a seismic chimney (SC), is observed beneath this region (Fig. 5a).

Unit 3: Unit 3 comprises stratified, relatively undisturbed sediments with a slight northwestward dip, extending to ~1.2 km depth. Reflections are generally continuous but attenuate with increasing depth and towards the northwest (Fig. 5a), partly due

200 to processing artefacts. In the lower part of the seismic section, polarity reversals relative to the seafloor suggest the presence of gas-bearing sediments near the SC. Below ~1.1 km, reflections remain undisturbed beneath the seismic chimney.

4.2 P- and S-wave Velocities of Profile A

The derived Vp and Vs models for profile A are displayed in Fig. 5a and 5b, respectively and summarized in Table S1 in Supplement S1. Ray coverage and traveltime fits indicate a good agreement between the observed and modelled data, with a

205 high ray density for both wave types (Fig. S1 for Vp and S2 for Vs in Supplement S1).

Seismic velocities increase gradually with depth from 1510 m/s at the seafloor to 1900 m/s at ~1.2 km depth for P-waves, and from 140 m/s to 860 m/s for S-waves (Figs. 5 and 6). The water column is assigned a constant velocity of 1483 m/s. Both Vp and Vs show minimal lateral variation, resulting in laterally stable Vp/Vs-ratios within each layer. Within Unit 1 the Vp increase slightly from 1510 m/s beneath the seafloor to 1530 m/s in ~720 m depth, and the Vs from 140 m/s to 230 m/s,

210 respectively. This yields in a Vp/Vs-ratio decrease from 10.6 to 6.8. Within Unit 2 the Vp values exhibit a stronger increase from 1580 m/s to 1760 m/s at ~880 m depth, and Vs from 320 m/s to 460 m/s, respectively. The resulting Vp/Vs-ratios decrease from 5 to 3.8. In the lowermost part, Unit 3, the seismic velocities follow the same trend, Vp increase from
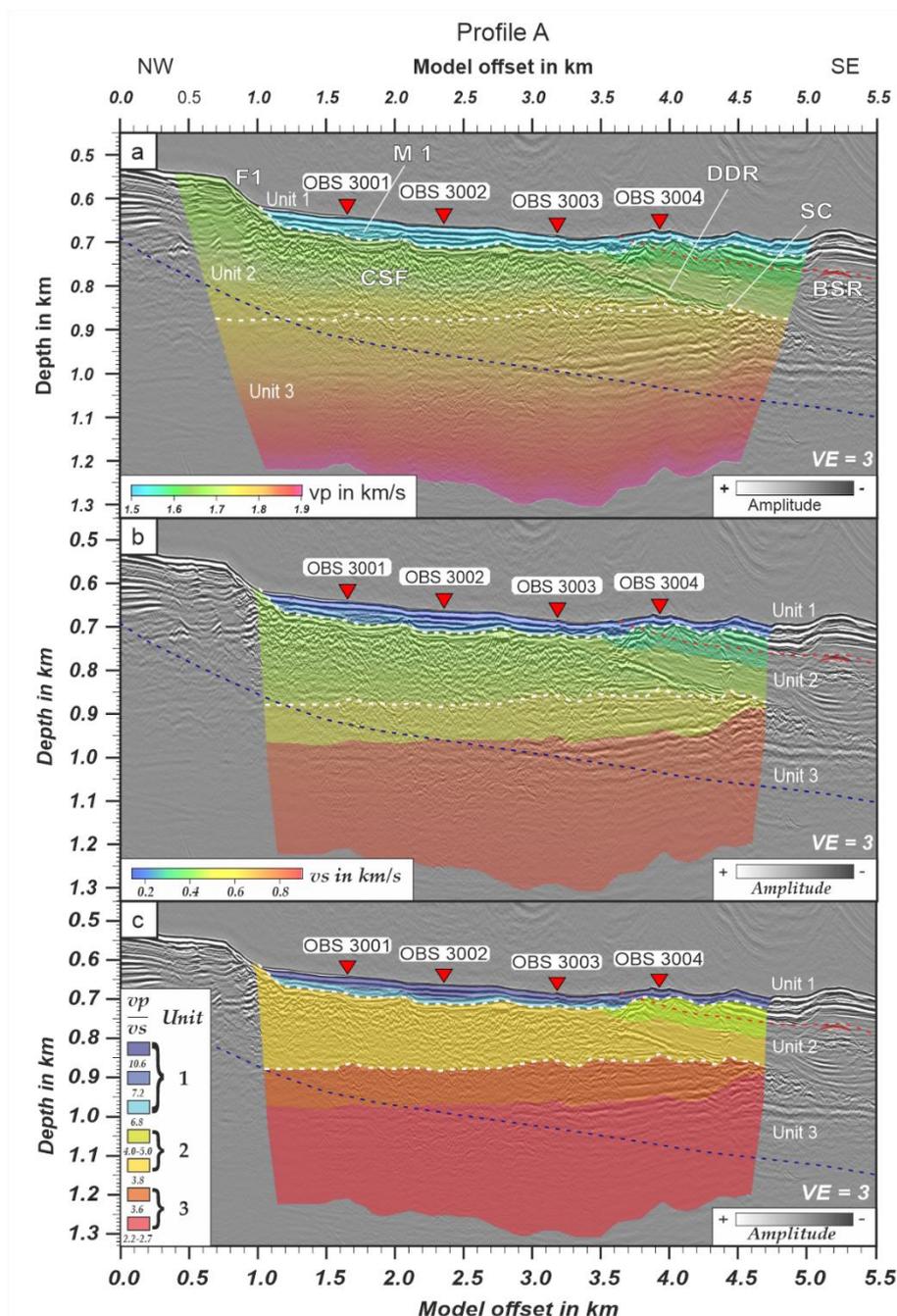
Fig. 5: Seismic velocity structure models of profile A. (a) P-wave velocity, (b) S-wave velocity, and the corresponding (c) Vp/Vs-ratio models overlaying the 2-D MCS seismic data. The seismic section is vertically exaggerated by a factor of three. Inverted red triangles indicate the position of the OBSs along the profile. Seismic anomalies are pointed out: BSR – bottom-simulating reflector, CSF – chaotic seismic facies, DDR – downward dipping reflector, F1 – fault, M1 – MTD, and SC – seismic chimney structure. The dashed white lines mark the boundaries of Unit 2. The dotted red line marks the theoretical base of the present-day GHSZ, calculated using a bottom- water temperature of 9° C and a geothermal gradient of 22 °C/km. The blue dotted line indicates the estimated GHSZ base during the Last Glacial Maximum (LGM), assuming a bottom temperature of 4 °C and the same thermal gradient (both after Badhani, 2016).

1760 m/s to 1900 m/s in ~1.2 km depth, and Vs from 500 m/s to 860 m/s, yielding in a Vp/Vs-ratio decrease from 3.6 to 2.2.

215 The DDR, marking a structural boundary, coincides with a noticeable 80 m/s velocity drop in Vp, and a normal-polarity amplitude reflection, indicative of lithological contrast (Fig. 6).
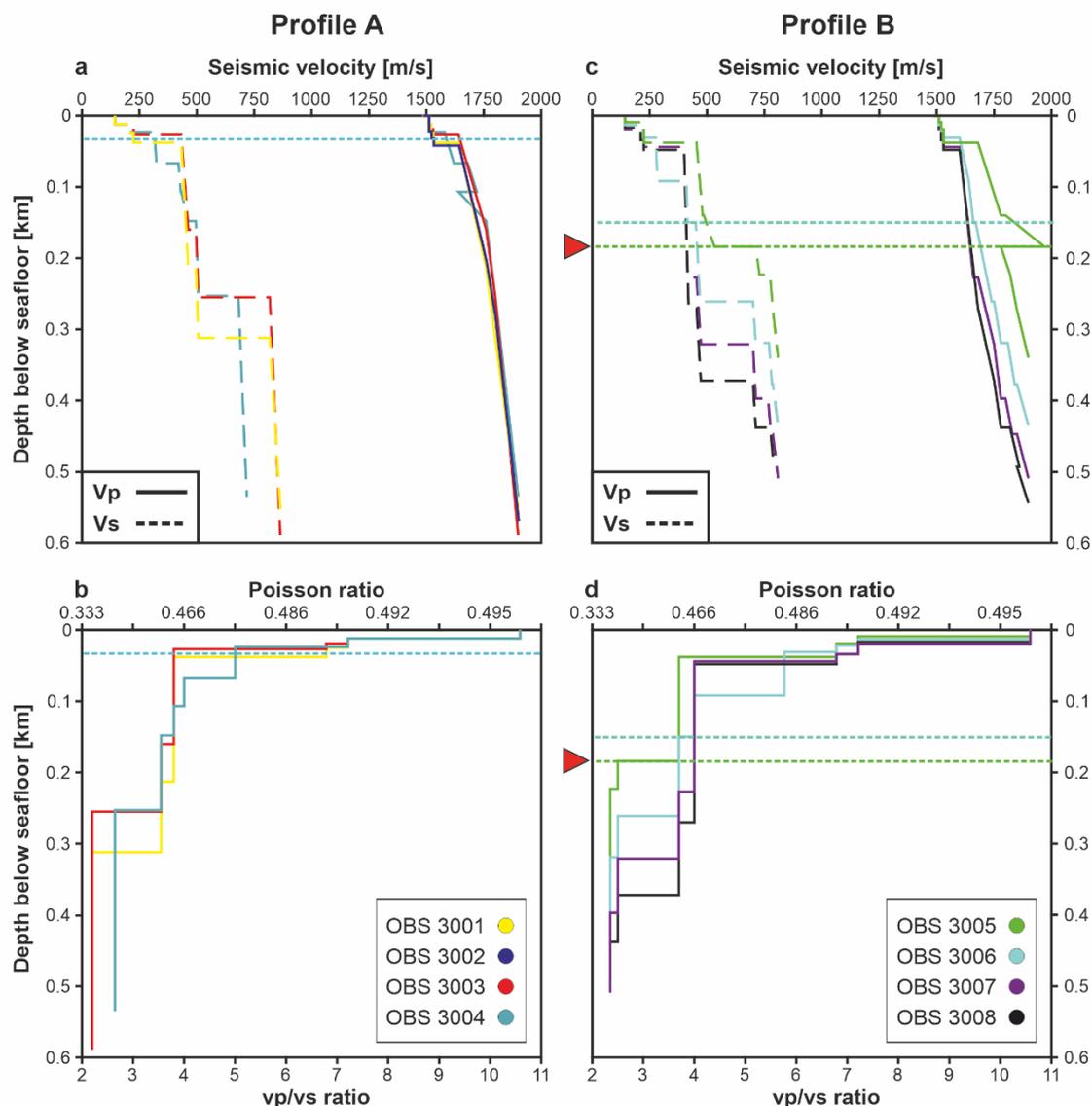

Fig. 6: 1-D velocity and ratio profiles for OBS stations along profiles A and B. (a) 1-D P-wave (solid lines) and S-wave (dashed lines) velocity profiles for OBSs 3001-3004 along profile A. (b) Corresponding 1-D Vp/Vs and Poisson's ratios. Note: Poisson's ratio is non-linearly related to the Vp/Vs-ratio. (c) 1-D P-wave (solid lines) and S-wave (dashed lines) velocity profiles for OBSs 3005-3008 along profile B. (d) Corresponding 1-D Vp/Vs and Poisson's ratios. The horizontally dashed lines represent the theoretical base of the GHSZ (after Badhani, 2016) and the red triangle marks the observed BSR depth at OBS 3005.

4.3 Subsurface Structure of Profile B

Profile B crosses a steeper terrain compared to profile A, intersecting the slope failure zone near the NNE sidewall and extending southeast across a gully entering the S2 canyon (Fig. 2). Based on traveltime picking and final modelling, the
220   subsurface is divided again into three units, which are consistent with the units from profile A (Fig. 7). The units comprise of eleven model layers (B1-B11), with B1 representing the water column (more details regarding the layers in Supplement S1).

Unit 1: Unit 1 is characterised by continuous high-amplitude reflections and varying thicknesses (Fig. 7a). Northwest of the slump scar (0-1.8 km model offset), reflections are intact and well stratified (~100 m thick), resembling headwall strata in profile A. Within the slump scar (2.7 km model offset to profile end), reflections persist but unit thickness reduces from ~50 m
225   to ~30 m. Between 1.8 to 2.7 km model offset, horizons are disrupted by two normal faults (F2 and F3) reaching ~100 m below seafloor. These faults bound the upper extent of a chaotic seismic facies (CSF), suggesting sediment disturbance likely due to slumping.

Unit 2: CSF extends to ~900 m depth and bounds laterally between 1.8-3.7 km model offset (Fig. 7a). It terminates at the southeastern end against a lenticular structure (M2). This structure M2 exhibits semi-transparent internal reflections, and some
230   cross-cutting features interpreted as processing artefacts. Deformed reflections surround M2. Notably, active gas flares were observed in close proximity to faults F2 and F3 during the MSM-34 expedition (Bialas et al., 2014; Hillman et al., 2018), implying a potential vertical migration pathway for gas. Toward the northwest, the CSF is bound by a sequence of weakly reflective, sub-horizontal strata exhibiting a slight northwestward dip.

Two additional semi-transparent seismic bodies, M3 and M4, are embedded within a background of well-stratified, sub-
235   horizontal reflections. M3 forms an elongated, lens-shaped body marked by a ~20-30 m topographic step. It extends from ~4.0 km (OBS 3005) to 5.2 km model offset at a depth of ~850 m. A prominent reflector demarcates the base of M3 and separates it from the underlying body M4 (Fig. 7a). M4 spans from 3.7-5.4 km model offset, reaching a depth of ~950 m. Its thickness increases from ~50 m to 70 m in the southeast direction. Internally, M4 displays deformed reflections and localised zones of elevated amplitude, which may indicate gas-charged sediments. Reflectivity to the northwest of M3 and M4
240   diminishes gradually, possibly due to attenuation effects from gas presence.

Further southeast of 5.4 km model offset, the MCS data reveal several V-shaped reflectors extending downward from the seafloor to ~1 km depth. These are interpreted as processing artefacts due to their inconsistent geometry and lack of stratigraphic continuity.

Unit 3: A strong upward-bending reflector interpreted as BSR1 marks the top of Unit 3 (Fig. 7a and 7c). It crosscuts the
245   surrounding strata, shows reversed polarity, and mimics the seafloor. Enhanced, reversed-polarity reflections below BSR1 indicate potential gas accumulations. A second, weaker BSR (BSR2) is identified at ~1050 m depth (Fig. 7a). The layers beneath the BSRs display horizontal, stratified reflections with northwestward amplitude decay, indicating intact sediment.
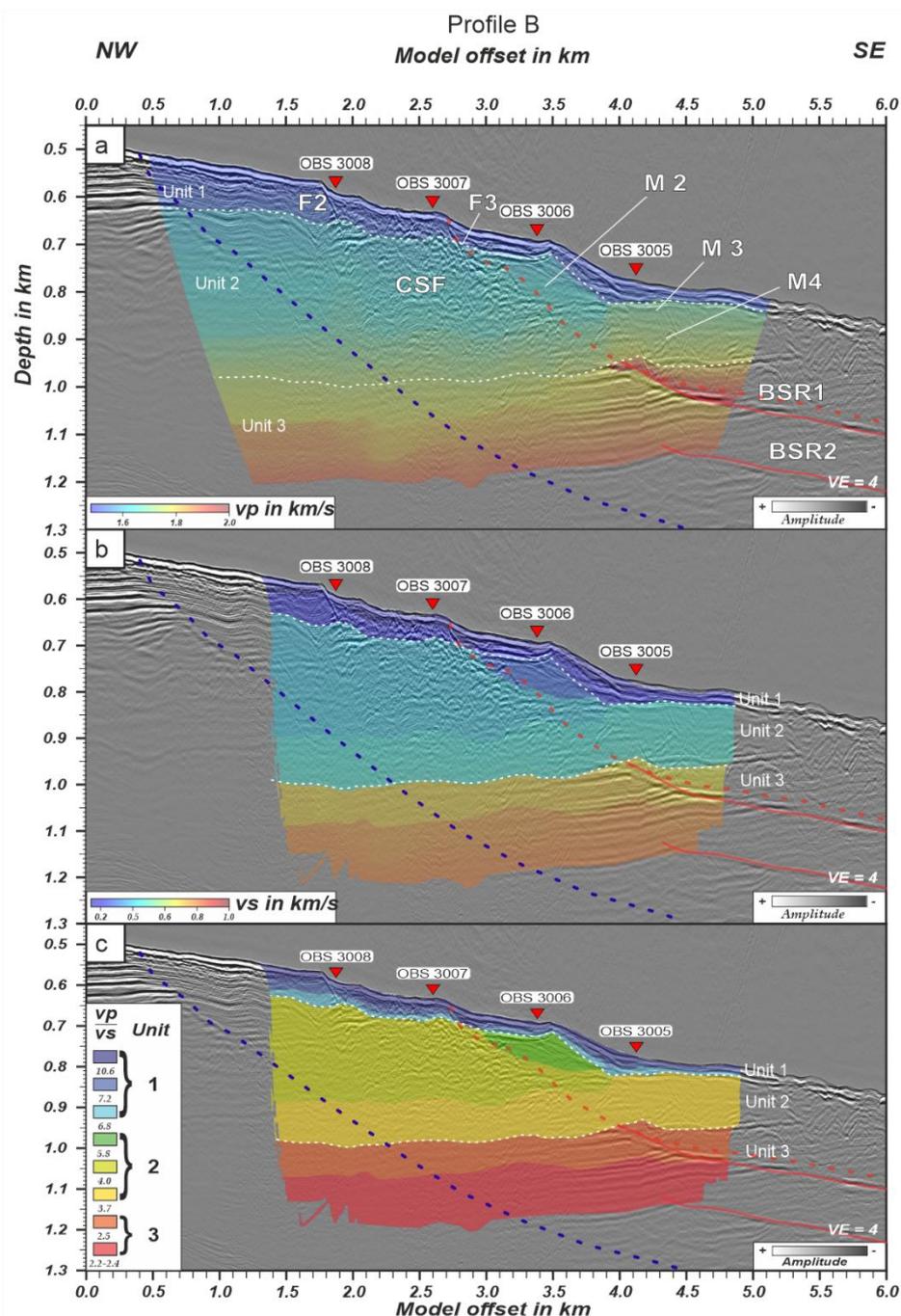
13

Fig. 7: Seismic velocity structure models of profile B. (a) P-wave velocity, (b) S-wave velocity, and the corresponding (c) Vp/Vs-ratio models overlaying the 2-D MCS seismic data. The seismic section is vertically exaggerated by a factor of three. Inverted red triangles indicate the position of the OBSs along the profile. Seismic anomalies are pointed out: BSR – bottom-simulating-reflector, CSF – chaotic seismic facies, F2 and F3 – fault, and M2 to M4 – MTD. The dashed white lines mark the boundaries of Unit 2. The dotted red line marks the theoretical base of the present-day GHSZ, calculated using a bottom- water temperature of 9° C and a geothermal gradient of 22 °C/km. The blue dotted line indicates the estimated GHSZ base during the Last Glacial Maximum (LGM), assuming a bottom temperature of 4 °C and the same thermal gradient (both after Badhani, 2016).

4.4 P- and S-wave Velocities of Profile B

250 The derived Vp and Vs models for profile B are displayed in Fig. 7a and 7b, respectively and summarized in Table S2 in Supplement S1. Ray coverage and traveltime fits indicate a good agreement between the observed and modelled data, with a high ray density for both wave types (Fig. S3 for Vp and S4 for Vs in Supplement S1).

Velocity models along profile B show a similar depth-dependent trend as in profile A, with gradual velocity increases from 1510 m/s at the seafloor to 1900 m/s at ~1.15 km depth (for Vp) and from 140 m/s to 810 m/s (for Vs), respectively. The water

255 column (B1) retains a constant velocity of 1483 m/s. Vp/Vs-ratios decrease with depth from 10.6 to 6.8 and remain laterally stable (Fig. 7c). Distinct from profile A, a velocity inversion is observed at BSR1 with a 190 m/s drop, while Vs remains largely unchanged, yielding in a Vp/Vs-ratio of 2.5. Velocities below BSR2 are beyond the model's coverage.

Within Unit 1 the Vp increase slightly from 1510 m/s beneath the seafloor to 1530 m/s within a depth range of 50-100 m, and the Vs from 140 m/s to 230 m/s, respectively. This yields in a Vp/Vs-ratio decrease from 10.6 to 6.8. Within Unit 2 the Vp

260 values exhibit a stronger increase from 1600 m/s to 1780 m/s at ~1 km depth, and Vs from 280 m/s to 480 m/s, respectively. The resulting Vp/Vs-ratios decrease from 5.8 to 3.7. In the lowermost part, Unit 3, the seismic velocities follow the same trend, Vp increase from 1800 m/s to 1900 m/s in ~1.2 km depth, and Vs from 490 m/s to 810 m/s, yielding in a Vp/Vs-ratio decrease from 3.7 to 2.4.

4.5 Constraints and Model Uncertainties

265 Phase picking and trial-and-error forward modelling are inherently involve subjective interpretation, contributing to the non-uniqueness of the final velocity models (Diehl, 2008). Model quality was assessed using ray coverage (Supplement S1), parameter sensitivity tests, and statistical metrics (Zelt, 1999).

Ray coverage is constrained by the number of OBS stations and the maximum offset of phase identification (~1.2 km). Depth nodes are densely spaced in the upper section (10 m) and coarser in the lower section (100 m), supporting high sensitivity near

270 the surface. Lateral spacing of velocity nodes varies between 100 and 500 m. Ray density reflects both resolution and smoothness and is generally high across the profiles (Figs. S1.1-S1.4 in Supplement S1). Picking uncertainty increases with depth, ranging from 5 ms to 24 ms (Tables S1 and S2 in Supplement S1), and is lower for P-waves due to their stronger signal and higher frequency content. Traveltime misfits between observed and synthetic arrivals show good agreement, supporting the consistency of the final models along both profiles.

275 Single-parameter sensitivity tests were conducted by perturbing top and bottom velocities within individual layers while keeping the gradient constant. Resulting traveltimes were compared to the observed picks to determine the maximum allowable perturbation still within the uncertainty window. This procedure was applied to Vp, Vp/Vs-ratios, and depth nodes. Vs uncertainties were derived using error propagation, accounting for the dependency on Vp and Vp/Vs-ratio.

Uncertainty ranges are as follows: (1) 1-7 % (10-100 m/s) for P-wave models, (2) 1-3 % (10-50 m/s) when incorporating S-
280 waves, (3) 1-9 % (±0.031-0.707) for the Vp/Vs-ratio, (4) 2-14 % (8-30 m/s) for the S-wave models, and (5) a 1-2 m depth
sensitivity. Perturbations were applied layer-wise; effects on adjacent layers were not included.

Statistical measures of model quality include Root-Mean-Square (RMS) traveltime residuals and normalised χ^2-values (Zelt
and Smith, 1992). Model A has an RMS traveltime residual of 3 ms and a normalised χ^2-value of 0.27 by using 8192 picks for
the analysis and the previously determined pick uncertainties (Table 1). Model B has an RMS traveltime residual of 4 ms and
285 a χ^2-value of 0.33 by using 10,063 picks and the corresponding pick uncertainties (Table 2). Pick uncertainties influence χ^2 by
controlling the allowable misfit between observed and synthetic traveltimes. The low χ^2 values obtained here reflect well-
constrained fits, supported by the use of conservative uncertainty estimates. The frequency-dependent effects of filtering (0-
20 Hz for S-waves, and 20-40 Hz for P-waves) suppress high-frequency noise and emphasise the stable, low-frequency signal
content that improves the reliability of traveltime picking.

290 5 Discussion

This study's OBS-MCS profiles span the central (profile A) and eastern (profile B) parts of the S2 slope failure zone. Building
upon previous velocity observations from the Danube Fan (e.g., Popescu et al., 2006; Zander et al., 2017; Bialas et al., 2020a)
and MeBo200 drilling results (Riedel et al., 2020; Bohrmann et al., 2018), our data reveal key processes driving slope
instability, including lithostratigraphic underconsolidation, focused fluid migration, gas hydrate dynamics, and the distribution
295 of MTDs.

5.1 Sedimentary Architecture

Seismic velocities and the integrated OBS-MCS data reveal systematically low P-wave velocities and elevated Vp/Vs-ratios
in the shallow subsurface (Fig. 5 and 7, Tables S1 and S2 in Supplement S1), reflecting water-rich clays and silts with poor
consolidation (Sava and Hardage, 2009; Hamilton, 1979). These properties are consistent with rapid burial, limited dewatering,
300 and a predominance of fine-grained, organic-rich sediments typical of the Danube Fan. Drilling results from the MeBo200
campaign confirm the presence of hemipelagic clays and silts, interbedded with sandy levee deposits with high porosity and
low shear strength (Bohrmann et al., 2018; Riedel et al., 2020), highlighting the metastable mechanical state of the deposited
units. Even with depth-dependent compaction, the measured seismic velocities remain below the values expected for normally
consolidated marine sediments (Hamilton, 1979), underlining the preservation of underconsolidation as a primary factor
305 controlling the slope stability.

The upper sedimentary drape (Unit 1) shows well-stratified, high-amplitude reflections but seems to have low shear strength.
Intercalated MTDs, such as the lens-shaped body M1 on profile A (Fig. 8), record past slope failures that infilled depressions
near the headwall (e.g., Schnellmann et al., 2006). On profile B, disturbed high-amplitude reflections confined between faults
F2 and F3 (Fig. 9) point to downward-slipping sediments adjacent to the sidewall. The chaotic seismic facies in Unit 2
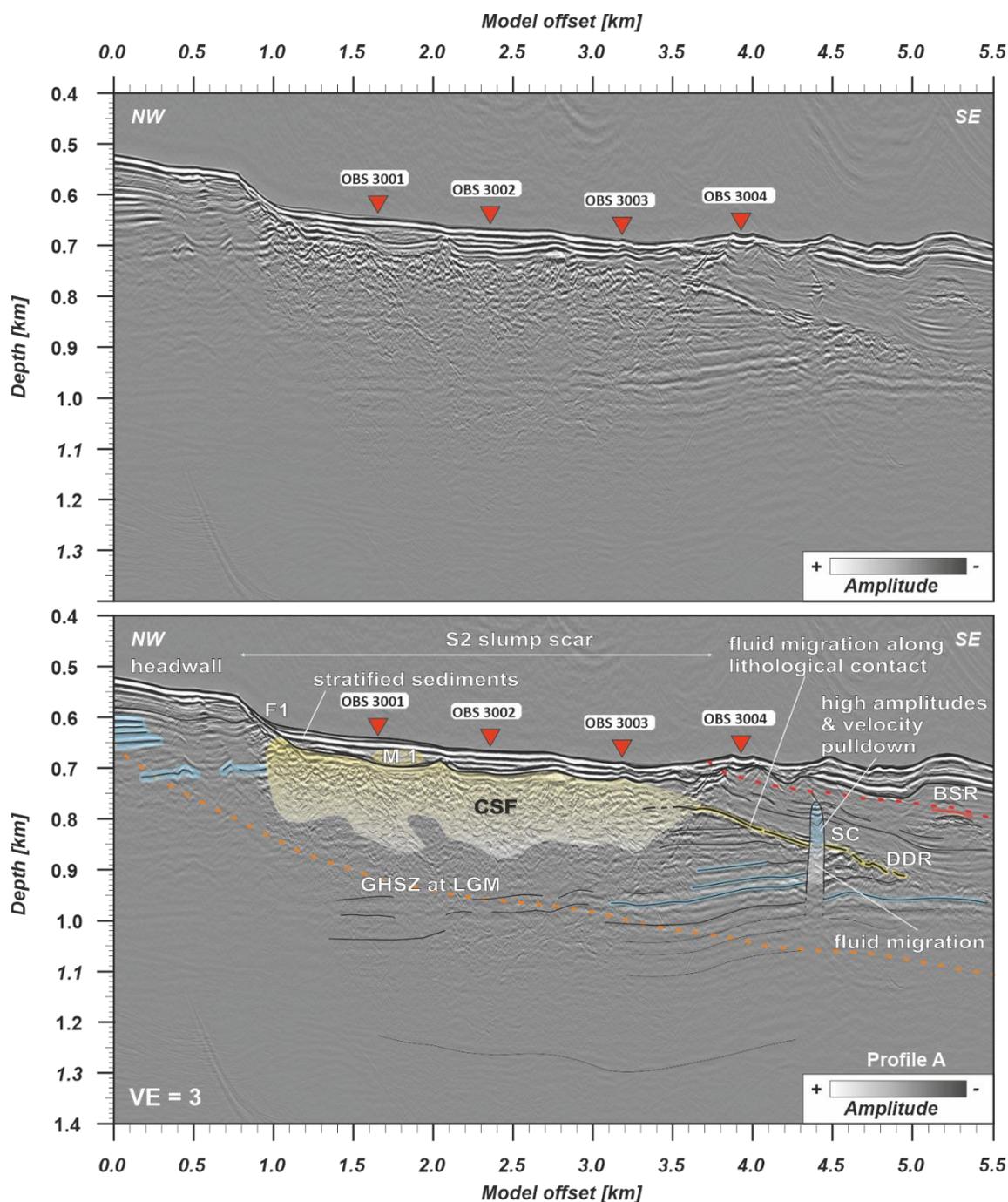
16

Figure 8: Seismic section (upper panel) and interpretation (lower panel) of high-resolution MCS profile A. Gas-charged zones are shaded in light blue. Small-scale mass-transport deposits (MTDs), including M1 and chaotic seismic facies (CSF1), bottom-simulating reflector (BSR), as well as the lithological boundary DDR (downward-dipping reflector), are highlighted in yellow. A seismic chimney (SC) is visible southeast of OBS 3004. The dotted red line marks the theoretical base of the present-day GHSZ, calculated using a bottom-water temperature of 9° C and a geothermal gradient of 22 °C/km. The orange dotted line indicates the estimated GHSZ base during the Last Glacial Maximum (LGM), assuming a bottom temperature of 4 °C and the same thermal gradient (both after Badhani, 2016).
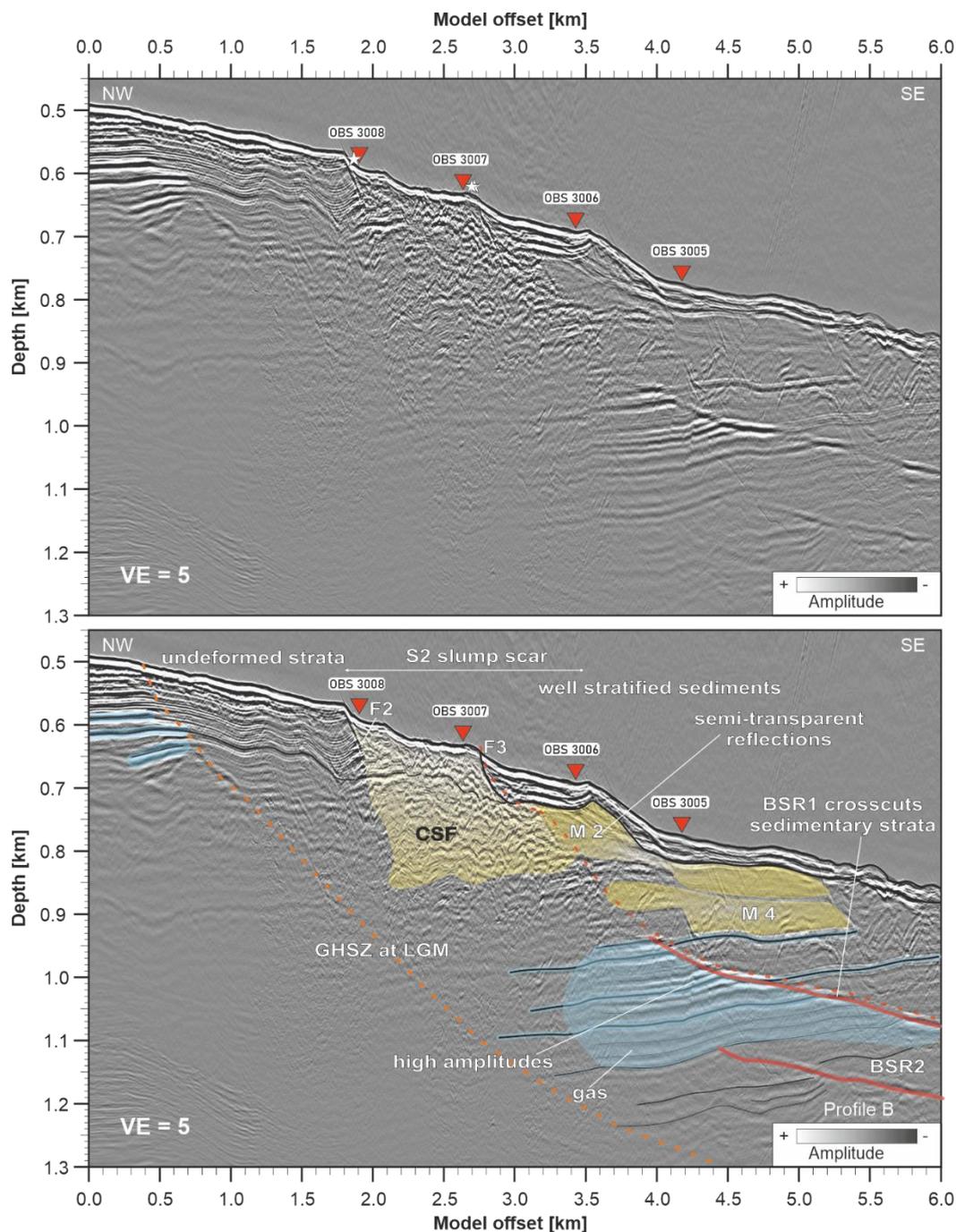
310

Figure 9: Seismic section (upper panel) and interpretation of high-resolution MCS profile B. Gas-charged zones are highlighted in light blue, while small-scale MTDs, including M2, M3, and chaotic seismic facies (CSF2), are marked in yellow. Solid red lines indicate BSRs. The dotted red line marks the theoretical base of the present-day GHSZ, based on a bottom-water temperature of 9 °C and a geothermal gradient of 22 °C/km. The dotted orange line shows the inferred base of the GHSZ during the Last Glacial Maximum (LGM), assuming a bottom-water temperature of 4 °C (both after Badhani, 2016). White stars indicate gas flares observed during cruise MSM-34 (Hillman et al., 2018).

18

(Figs. 8 and 9) is characterised by disturbed and discontinuous reflections with an irregular upper boundary. It is interpreted as acoustic turbidity caused by sediment deformation linked to the S2 failure or even the remnants of this event (e.g., Vanneste et al., 2014; Chand and Minshull, 2003; Judd and Hovland, 1992). Their confinement within the slump scar supports a local

315 failure origin, pre-dating the deposition of Unit 1. Semi-transparent MTDs with normal-polarity tops and inverted-polarity bases (e.g., M2, M3 on profile B; Fig. 9) suggest vertical density contrasts from sediment mixing during material transport (Riedel et al., 2020; Mulder and Cochonat, 1996). Together, these deposits record a repeating cycle of failure, remobilisation, and redeposition.

Underlying sediments (Unit 3) represent older levee and overbank deposits associated with phases of active canyon

320 sedimentation. These are dominated by fine-grained clays and silts with minor sandy interbeds (Riedel et al., 2020; Bohrmann et al., 2018). Although compaction leads to a gradual seismic velocity increase with depth, the observed P-wave values remain lower than the reference values for normally consolidated sediments (Hamilton, 1979), suggesting ongoing underconsolidation in this slope region. This effect is attributed to the existence of highly fluid to plastic clays with a high-water content, resulting in a low shear strength and cohesion, high compressibility, and therefore, experience significant instability when disturbed

325 (Ivanik et al., 2025; Ballas et al., 2018; Bartetzko and Kopf, 2007; Keller, 1982). Such mechanically weak levee sequences are highly prone to slope instability under changes in pore pressure or external loading (Mitchell and Soga, 2005). The stratigraphic architecture, levee deposits capped by hemipelagic deposits and overprinted MTDs, generates a heterogeneous depositional environment. Along the boundaries between silt deposits and levee sequences, the mechanical contrast generates localised stress concentrations (Ivanik et al., 2025).

330 Normal faults (F1-F3) mapped in the upper ~100 m (Figs. 8 and 9) penetrate only the shallow units but likely serve as local zones of structural weakness and potential fluid migration pathways (e.g., Hillman et al., 2018). Moreover, chaotic facies and porosity contrasts in sand-rich interbedded layers within otherwise fine-grained sediments act as mechanical discontinuities. These heterogeneities reflect both the record of past instability and structural predisposition for future slope instability under stress redistribution or pore pressure changes.

335 The sedimentary architecture of the S2 slope area in the Danube Fan is dominated by fine-grained, underconsolidated sediments deposited in a rapidly accumulating deltaic fan system. High Vp/Vs-ratios, mechanically weak clays and silts, interbedded MTDs, and widespread underconsolidation define a slope prone to failure.

5.2 Gas Migration and Hydrate Dynamics

Gas migration and hydrate processes in the Danube Fan are closely linked to the fine-grained underconsolidated sedimentary

340 architecture described above. Seismic observations reveal a dynamic interplay between free gas occurrence, focused fluid pathways, and transient gas hydrate stability.

Seismic anomalies, including polarity reversals, abrupt amplitude changes, and velocity pull-downs, provide strong evidence of active and past gas migration. A prominent capped seismic chimney observed southeast of OBS 3004 (profile A; Fig. 8) intersects Unit 2 and terminates below the seafloor, suggesting vertical transport of gas-bearing fluids (Judd and Hovland,

345 2007). The chimney is associated with a velocity pull-down and high-amplitude capping reflections, both features commonly linked to local overpressure build-up or hydrate dissociation (Hillman et al., 2018; Judd and Hovland, 2007). Its vertical extent exceeds the present-day base of the GHSZ, indicating that gas migration may have been triggered by hydrate dissociation since the Last Glacial Maximum (Riedel et al., 2020, 2021a).

Additional seismic anomalies include polarity-reversed reflections beneath the downward-dipping reflector (DDR), and a drop
350 of ~80 m/s in the Vp (Fig. 5a; Table S1 in Supplement S1). These features strongly suggest free gas accumulation in porous, sand-rich horizons sealed by low-permeability silts and clays (Riedel et al., 2020; Sava and Hardage, 2009). This is further supported by polarity-reversed, high-amplitude horizons on top of the S2 slope failure site that indicate previous gas charging. Such stratigraphically confined accumulations highlight the role of lithological layering and permeability contrasts in controlling gas distribution.

355 During cruise MSM-34, several active gas flares were detected near the faults F2 and F3, along the headwall, and the southeast sidewall, including sites only ~40 m from OBS 3004 (Hillman et al., 2018; Bialas et al., 2014). Additional gas flares within the slump scar were revealed at water depths shallower than the predicted GHSZ (Fig.2), and coincide with vertical fluid escape structures, such as seismic chimneys and disrupted, gas-bearing horizons (Hillman et al., 2018). Even though there is no clear seismic evidence along the profiles analysed confirming faults as active conduits, suggesting that gas escape is more
360 likely episodic and localised similar to the situation at Hydrate Ridge off Oregon (Crutchley et al., 2013) and Formosa Ridge off Taiwan (Kunath et al., 2022). To generate such vertical structures, the gas concentration has to exceed hydrostatic pressure and capillary entry pressures (Løseth et al., 2009; Judd and Hovland, 2007). The microbial degradation of organic-rich sediments supplied by hemipelagic and turbiditic input is the most plausible gas source (Popescu et al., 2006; Jørgensen et al., 2004; Winguth et al., 2000). Thermogenic contributions from deeper reservoirs, common in other deltaic hydrate provinces
365 (such as the Mississippi Fan; Madof et al., 2019; Sassen et al., 2001), are not supported within the Danube Fan (Starostenko et al., 2010). Gas hydrate dissociation could contribute to an episodic increase in gas concentrations.

BSRs with reversed polarity are present in profile B (Fig. 9) and can be interpreted as a direct indicator for the presence of gas hydrates (Boswell et al., 2016). However, their discontinuous character, combined with observed velocity reduction of up to - 190 m/s across the upper BSR (Figs. 7 and 9, Table S2 in Supplement S1), indicates that it primarily reflects free gas beneath
370 the base of the GHSZ rather than significant hydrate accumulation (e.g., Andreassen et al., 2003).

Recent numerical modelling studies of the Danube paleo-delta hydrate system by Gupta et al. (2024) provide valuable context for the transient and patchy nature of gas hydrate stability observed here. Their simulations highlight the sensitivity of hydrate formation and dissociation to sedimentation sequences and methane phase transition kinetics, which control the dynamic behaviour of hydrate stability in this setting. This explains the observed discontinuous and stacked BSRs, attributed to narrow
375 windows of hydrate formation and dissociation rates that limit hydrate accumulation and promote the coexistence of free gas beneath the GHSZ. Such dynamic processes are consistent with recent modelling emphasising how sedimentation rates and methane phase transitions drive transient hydrate systems (e.g., Iemelianov et al., 2025). Together, these findings support the

interpretation of a hydrate-poor but gas-active system undergoing ongoing re-equilibration since the LGM, prone to episodic venting and overpressure.

380 Local phase reversals at the intersection of BSRs and stratigraphic reflectors (Fig. 9) suggest that free gas may migrate into sand-rich layers. Nevertheless, the limited extent of these accumulations implies that gas concentrations are insufficient to overcome hydrostatic pressure and capillary entry forces for further migration (Judd and Hovland, 2007).

The thermally derived current base of the GHSZ lies ~20 m shallower than the observed BSR, suggesting a state of transient disequilibrium in the hydrate system (Burwicz-Galerne et al., 2024; Riedel et al., 2021a). This discrepancy suggests that

385 formerly trapped gas has migrated upwards, recharging shallower sediments. The transient disequilibrium state indicated by the observed BSR depth being deeper than the thermally derived GHSZ base aligns well with Gupta et al. (2024), who highlight how gas migration upward, triggered by hydrate dissociation and sediment loading, can cause dynamic fluctuations in hydrate stability and gas saturation over geological timescales. Such transient behaviour likely drives episodic gas venting and overpressure build-up observed in seismic chimneys and fluid escape features, emphasizing the system's sensitivity to recent

390 environmental changes. The presence of multiple former BSRs preserved in the stratigraphy supports a history of dynamic hydrate re-equilibration since the LGM (Riedel et al., 2021a; Grevemeyer and Villinger, 2001) or rapid deposition of levee deposits next to the channel as reported elsewhere in the Danube Fan (Zander et al., 2017).

Controlled-source electromagnetic (CSEM) and drilling results indicate very low hydrate saturations, generally close to 0% within the GHSZ and <10% just at the interface of the BSR (Burwicz-Galerne et al., 2024; Bialas et al., 2020a; Schwalenberg

395 et al., 2020). Although slightly elevated P-wave velocities were observed (up to 1970 m/s above the BSR), the absence of corresponding Vs anomalies suggests only a small fraction of gas hydrates is present and disseminated within the sediment or patchy pore-filling (Priest et al., 2009; Yun et al., 2005). Importantly, within the resolution and uncertainties of our dataset, the lack of S-wave velocity anomalies indicates that hydrates are not acting as cementing phases at grain contacts. Instead, they occur as disseminated or patchy pore-filling accumulations that do not significantly alter bulk shear strength. This implies

400 that hydrate presence does not directly stabilise the sediment framework, and hydrate dissociation has no intrinsic weakening effect. Rather, the impact of hydrates on slope stability in this setting is indirect, operating mainly through dissociation-driven gas release and pore-pressure increase. This form of gas hydrate distribution does not significantly alter the bulk elastic properties of the host sediment. Gas release during MeBo200 drilling near the BSR (Bohrmann et al., 2018) further indicates hydrate destabilisation at shallow levels.

405 Gas migration in the S2 slope of the Danube Fan is controlled by stratigraphic and structural discontinuities, with sand-rich layers acting as preferred migration pathways (Gupta et al., 2024). Vertical transport is indicated by the seismic chimney, but it cannot be determined which impact such features have due to the limited observation. Free gas accumulations are locally trapped beneath low permeability seals and seem to periodically discharge through venting, while hydrate presence is minimal and dynamically re-equilibrating in response to post-glacial conditional changes. Despite the presence of BSRs with reversed

410 polarity, their discontinuous nature and limited hydrate saturation (<10%) suggest a predominantly hydrate-poor system where free gas accumulates beneath the base of the GHSZ in porous sand horizons sealed by low-permeability layers. This hydrate-

poor but gas-active environment promotes localised overpressure and episodic venting, contributing to slope instability and complex methane migration pathways within the Danube Fan.

5.3 Geohazard and Slope Instability

415 The combination of underconsolidated sediments, focused gas migration, and weak mechanical layering creates a slope system prone to failure in the Danube Fan. Results from the OBS-MCS integrated analysis, MeBo200 drilling, and core analysis support this assumption.

The S2 slope failure zone is bounded by a prominent horse-shoe shaped headwall (Fig. 2), documenting a major mass-wasting event (Hillman et al., 2018). Within this zone, chaotic seismic facies and multiple MTDs record past slope failure episodes

420 (Riedel et al., 2020; Vanneste et al., 2014). Although shallow faults (F1-F3) only penetrate the upper ~100 m, they represent structural weaknesses that may act as local failure initiation points, particularly where overpressured gas or fluids accumulate (Hillman et al., 2018).

Potential triggers include (1) rapid sedimentation loading during phases of canyon activity, (2) earthquakes, (3) overpressure development through gas charging and hydrate dissociation, and (4) reduction in effective stress due to excess pore pressure

425 in clays and silts (Gupta et al., 2024; Urlaub et al., 2013; Mitchell and Soga, 2005). These triggers range from gradual preconditioning by underconsolidation to episodic external forcing. The role of gas hydrate dissociation in promoting localized overpressure and slope instability has been increasingly recognized in recent numerical and thermodynamic models (Iemelianov et al., 2025). Our integrated seismic and drilling evidence supports this mechanism as a key driver in weakening the underconsolidated sedimentary sequence, thereby enhancing slope failure susceptibility.

430 Seismic velocity profiles consistently show lower-than-expected P-wave velocities compared to normally consolidated reference curves (Hamilton, 1979), underscoring prevailing underconsolidation throughout Units 1-3. This condition is confirmed by drilling, which revealed high porosities and clay-rich levee deposits with low undrained shear strength (Riedel et al., 2020; Bohrmann et al., 2018). Such sediments are prone to strength reduction upon external forcing (Gupta et al., 2024; Ballas et al., 2018; Keller, 1982), amplifying slope failure instability.

435 Localised free gas accumulations, as evidenced by polarity reversals and velocity pull-downs (Riedel et al., 2020; Sava and Hardage, 2009), further contribute to elevated pore pressures. Chimneys and disrupted horizons demonstrate focused zones of fluid migration, redistributing overpressure vertically and laterally across the slope area (Løseth et al., 2009; Judd and Hovland, 2007). Overpressure conditions in such weak sediments reduce the effective stress and can lead to failure propagation across mechanically layered sequences.

440 Integrated OBS-MCS seismic data and MeBo200 ground-truth data provide complementary evidence for slope instability. OBS results show shallow velocity anomalies associated with chimneys and DDR-related gas accumulations, while cores confirm the presence of mousse-like, homogeneous silty clays in chaotic facies (Riedel et al., 2020; Bohrmann et al., 2018). These deposits lack internal layering and exhibit reduced shear strength, consistent with mass-transport deposits and disturbed slope material. This suggests that localised material and porosity contrasts, rather than gas accumulations, are the key factors

445   regarding slope stability. Together, these data point to a slope system, where stress redistribution and underconsolidation are critical factors controlling failure dynamics.

The geohazard potential of the S2 slope is high, based on the combined effects of (1) weak, underconsolidated clays and silts; (2) stratigraphic discontinuities and shallow faults acting as planes of weakness; and (3) localised overpressure from gas accumulation and hydrate disequilibrium. These conditions suggest that even moderate external triggers, such as sediment

450   loading or regional seismicity, may be sufficient to induce slope failure.

5.4 Comparative Fluid Systems in Continental Margin Fans

Deltaic deep-water fan systems elsewhere show closely comparable controls on underconsolidation and mechanical weakness. The Danube Fan is situated on a passive continental margin of the northwestern Black Sea (Fig. 1), shaped by Pleistocene fluvial influx and hemipelagic sedimentation under a tectonically quiescent regime, with no evidence of significant

455   deformation (Popescu et al., 2001; Winguth et al., 2000). Gas-migration indicators and hydrate behaviour in other systems place the Danube Fan as an endmember case.

The Amazonas Fan, also on a passive margin, is driven by massive sediment supply from the Amazon River, producing thick channel–levee complexes and frequent MTDs (Maslin, 2009; Cobbold et al., 2004). Fine-grained levee deposits (mostly silts

460   and clays) promote undersconsolidation and reduced shear strength (Ketzer et al., 2018), while continuous discharge and channel migration generate lithologic heterogeneity and local instability (Souza et al., 2025; Maslin, 2009; Audet, 1998; Flood et al., 1991). Thermogenic-derived hydrocarbons increase the fluid overpressure (Cobbold et al., 2004). BSRs, chimney structures, and widespread venting from within the GHSZ show an active hydrate-free-gas system and transient hydrate stability, with direct hydrate recoveries reported (Praeg et al., 2022; Ketzer et al., 2018). Fault-controlled gas migration forms

465   gas-charged zones with low seismic velocity and acoustic wipeouts, which correspond to weak layers (Ketzer et al., 2018). Gas hydrate concentrations can strengthen the levee deposits initially (e.g., Priest et al., 2009; Yun et al., 2005). Evidence for gas hydrates within the GHSZ is largely inferred from cores presenting different gas hydrate distributions at vent-proximal sites and levee settings (Ketzer et al., 2018). While at vent-proximal sites, nodular to massive types occur, gas hydrates within the levee deposits are rather disseminated, pointing to low-concentrations (Ketzer et al., 2018). But the dissociation of these

470   low concentrated gas hydrates can reduce the shear strength and raises the pore pressure within these deposits, destabilising slopes (Praeg et al., 2022; Ketzer et al., 2018). Those zones are commonly associated with MTDs, indicating past slope failures. The combined effects of hydrate dissociation, pore pressure buildup, and gas-related weakening make the Amazonas Fan particularly prone to submarine landslides, even on gentle slopes.

475   The Krishna-Godavari Basin is located on a rifted passive margin, where Early Cretaceous rifting superimposed on older Gondwana-age graben systems created a horst-graben architecture (Radhakrishna et al., 2012; Rao, 2001). Thick, rapidly deposited sediments form sand-rich channel-levee deposits embedded in a mud-rich surrounding (Collett et al., 2008, 2019;

Kumar et al., 2014). Rapid sediment accumulation and limited dewatering lead to low shear strength and localised overpressure zones, especially in the graben structures (Collett et al., 2019; Chatterjee et al., 2011; Riedel et al., 2010). Inside the Krishna-

480   Godavari Basin, occasionally gas hydrates occur as fracture-filling hydrates in clay-silt-rich sections (Collett et al., 2014), but predominantly as laterally extensive, sand-hosted, pore-filling systems within the GHSZ (Collett et al., 2019). Inside the sandy levee deposits the gas hydrate concentration is locally very high (>50%, occasionally ~80%), with free gas accumulations beneath (Collett et al., 2008, 2019; Riedel et al., 2010). These conditions create strong contrasts between the hydrate-bearing sands and the weak surrounding mud, enhancing slope failure potential. Large-scale slope failures, including an ~11 km³ event,

485   confirm the high geohazard risk (Dewangan et al., 2025). Together, these factors make the Krishna-Godavari Basin a geohazard-prone margin where sediment instability is closely linked to complex structural settings, rapid sedimentation, and dynamic gas hydrate systems.

The Mississippi Fan, located in the Gulf of Mexico, is strongly influenced by salt tectonics; evaporites deform extensively to

490   form salt diapirs and structural pathways (Boswell et al., 2012; Sassen et al., 2001). The fan lobes are the major structural elements within the fan system (Twichell, 2009). They comprise a sandy channel base, silty-clayey overbanks, sheeted sands, with repeated levee failures linked to fluid migration and undrained loading of low-permeability muds (Damuth and Olson, 2015; Twichell, 2009; Weimer, 1990). The Gulf of Mexico Gas Hydrate Joint Industry Project (JIP) Leg II confirmed high-saturation pore-filling hydrates in thin-bedded to stacked turbidite sands (e.g., Haines et al., 2017). The hydrate saturations are

495   locally up to ~80% of the pore space near the base of the GHSZ and are sourced largely by deep thermogenic systems and focused along salt-related faults (Madof et al., 2019; Boswell et al., 2012). In adjacent clay-rich sections, gas hydrates occur primarily as fracture-fill, mostly veins, rather than pore-filling (Lee and Collett, 2012). Dissociation or free-gas build-up beneath sealing layers can reduce effective stress reduction and destabilise slopes (e.g., Madof et al., 2019). These factors make the Mississippi Fan a complex and potentially unstable system where salt tectonics, fluid migration, and high-saturation

500   gas hydrates significantly influence slope stability.

Taken together, these systems define a spectrum of hydrate–slope interactions. The Amazonas, Krishna–Godavari, and Mississippi fans are hydrate-rich, with sand-prone channel–levees and structural pathways concentrating fluids and free gas. In these settings, hydrate formation may initially enhance sediment strength, but dissociation typically drives pore-pressure

505   build-up and slope failure. Among them, the Amazonas Fan is the most prone to instability due to widespread hydrates, free gas, and fault-focused migration. The Krishna–Godavari Basin follows, where rift-related structures, rapid sedimentation, and hydrate-bearing sands interact to produce frequent failures. The Mississippi Fan occupies an intermediate position, with high-saturation hydrates in turbidite sands and salt-related pathways that localise overpressure and slope instability.

510   In contrast, the Danube Fan represents a hydrate-poor but gas-active endmember. Fine-grained, low-permeability levee and lobe sediments host patchy, low-saturation disseminated hydrates and shallow free-gas accumulations beneath BSR-like

24

horizons. Here, instability is governed primarily by underconsolidation and localised gas overpressure, with hydrates exerting a secondary influence. This highlights a distinct geohazard mode in which weak mud-dominated strata and diffuse gas charging control slope failure, rather than hydrate dissociation.

515   In summary, the comparison underscores that while hydrate-rich systems such as the Amazonas, Krishna–Godavari, and Mississippi fans face slope instability largely through hydrate dissociation and focused fluid migration, the Danube Fan demonstrates how slope failure can arise in hydrate-poor but gas-active margins. Across all systems, the hazard mechanism, weak layers, excess pore pressure, and external triggers, remains globally consistent, but the balance between hydrates, gas flux, and sediment properties dictates local failure behaviour and geohazard potential.

520   **6 Conclusion**

This study integrates high-resolution OBS-MCS seismic imaging with drilling and coring data to investigate sedimentary processes, fluid dynamics, and slope stability in the Danube Fan, northwestern Black Sea. The results demonstrate how weak sediment properties, localised fluid migration, and transient hydrate systems interact and affect the slope architecture and geohazard potential.

525

First, the S2 slope is dominated by rapidly deposited, underconsolidated mud-rich sequences that retain excess pore pressure due to incomplete dewatering. Elevated Vp/Vs ratios, low shear strength, and recurrent MTDs highlight how weak and heterogeneous layers precondition the slope to repeated failure.

530   Second, gas migration and hydrate behaviour exert a critical but have a secondary influence. Seismic anomalies, including chimneys, polarity reversals, and velocity pull-downs, reveal focused pathways for free gas, while hydrate occurrences are sparse, discontinuous, and low in saturation. Disequilibrium between observed BSRs and the predicted base of the GHSZ suggests a system still adjusting to post-glacial boundary conditions. In this hydrate-poor but gas-active margin, slope instability is governed more by gas overpressure within weak muds than by hydrate dissociation.

535

Third, the geohazard potential of the Danube Fan arises from the combined effects of underconsolidation, structural discontinuities, and localised overpressure. Within the resolution of our dataset, the lack of S-wave velocity anomalies indicates that hydrates do not act as cementing phases at grain contacts. Instead, they occur as sparse, patchy pore-filling accumulations that do not significantly alter bulk shear strength. Even moderate external triggers, sediment loading, earthquake
540   events, or minor hydrate destabilization can initiate slope failure, underscoring the sensitivity of this margin.

Placed in a global context, the Danube Fan defines one end of a spectrum of hydrate–slope interactions. Hydrate-rich systems such as the Amazonas, Mississippi, and Krishna–Godavari fans are dominated by sand-hosted pore-filling hydrates and

25

fracture-related accumulations that destabilise upon dissociation. By contrast, the Danube Fan is characterised by fine-grained lithologies, low-saturation disseminated hydrates, and diffuse microbial gas charging. Instability here reflects weak mud-dominated strata and gas overpressure rather than hydrate dissociation.

In conclusion, the Danube Fan exemplifies how sedimentary architecture, gas migration, and hydrate disequilibrium jointly govern slope stability in delta-fed margins. As a hydrate-poor but gas-active endmember, it advances understanding of Black Sea geohazards and provides a critical analogue for other underconsolidated, fine-grained continental margins in the early stages of hydrate system development.

Data Availability

The high-resolution MCS seismic profiles collected during MSM-34 within the SUGAR project framework (Bialas et al., 2014) are available from PANGAEA (Bialas et al., 2020a; Bialas and Riedel, 2020). The seismic lines were analysed and interpreted with IHS Kingdom® software. The corresponding OBS data are available from PANGAEA (Dannowski and Bialas, 2025). To identify the traveltimes derive the forward velocity model, the software packages PASTEUP and MODELING (Fujie, 2008b, a; Fujie et al., 2008) were used. The software is licensed under the GNU General Public Licence Version 2 and is available at https://www.jamstec.go.jp/obsmcs_db/e/software.html.

The bathymetric data were also acquired during MSM-34 cruise and are available from PANGAEA (Wintersteller and Bialas, 2016). Further, the facility of the National Oceanic and Atmospheric Administration's National Centers (NOAA) was used for access to ETOPO-1 bathymetric data and related metadata from the northwestern Black Sea (Amante and Eakins, 2009). The NOAA's bathymetric data are licensed under the Creative Commons CC0 license or CC BY 4.0 license. Maps and figures were created through Generic Mapping Tools (GMT) version 6 (Wessel et al., 2019a, b) licensed under LGPL version 3 or later, available at https://www.genericmapping-tools.org/. Figure were reworked or created with Corel Draw® Graphic Suite 2019.

The gas hydrate samples collected during the GHASS (Gas Hydrates, fluid Activities, and Sediment deformation in the western Black Sea) cruise are attributed to Ker and Riboulot (2015). The observed gas flares within the water column in the S2 slope failure zone are adapted from Hillman et al. (2018) and the MeBo200 drill sites are attributed to Riedel et al. (2020). Further, the estimated upper GHSZ boundary is adapted from Zander et al., (2017) and Riedel et al. (2020).

Author Contributions

HSH: conceptualization, formal analysis, methodology, validation, visualization, writing – original draft, writing – review and editing

AD: conceptualization, formal analysis, investigation, methodology, supervision, validation, writing – review and editing

JB: conceptualization, funding acquisition, investigation, methodology, project administration, resources, supervision, validation, visualization, writing – review and editing

FG: formal analysis, investigation, methodology, writing – review and editing

JH: formal analysis, investigation, methodology, writing – review and editing

DK: formal analysis, methodology, validation, writing – review and editing

CB: conceptualization, validation, methodology, resources, supervision, writing – review and editing

Competing Interests

We declare that we have no competing interest.

References

Amante, C. and Eakins, B. W.: ETOPO1 1 Arc-Minute Global Relief Model: Procedures, Data Sources and Analysis, https://doi.org/10.7289/V5C8276M, 2009.

Andreassen, K., Berteussen, Karl. A., Sognnes, H., Henneberg, K., Langhammer, J., and Mienert, J.: Multicomponent ocean bottom cable data in gas hydrate investigation offshore of Norway, J. Geophys. Res., 108, 2399, https://doi.org/10.1029/2002JB002245, 2003.

Audet, M. D.: Mechanical properties of terrigenous muds from levee systems on the Amazon Fan, SP, 129, 133–144, https://doi.org/10.1144/GSL.SP.1998.129.01.09, 1998.

600 Badhani, S.: Slope failure and gas hydrate dissociation in the Danube deep-sea fan, NW Black Sea, Master's Thesis, Christian-Albrechts-Universität zu Kiel, GEOMAR Helmholtz-Centre For Ocean Research Kiel, 88 pp., 2016.

Ballas, G., Garziglia, S., Sultan, N., Pelleter, E., Toucanne, S., Marsset, T., Riboulot, V., and Ker, S.: Influence of early diagenesis on geotechnical properties of clay sediments (Romania, Black Sea), Engineering Geology, 240, 175–188, https://doi.org/10.1016/j.enggeo.2018.04.019, 2018.

605 Bartetzko, A. and Kopf, A. J.: The relationship of undrained shear strength and porosity with depth in shallow (<50 m) marine sediments, Sedimentary Geology, 196, 235–249, https://doi.org/10.1016/j.sedgeo.2006.04.005, 2007.

Bialas, J. and Flueh, E. R.: Ocean bottom seismometers: New instrument packages demonstrates value of recording full wavefield; shows that interpretations of sediment shear wave velocities are reliable., Sea Technology, 40, 41–46, 1999.

Bialas, J. and Riedel, M.: 2D multichannel seismic profiles during Maria S. Merian cruise MSM34, Black Sea, 610 https://doi.org/10.1594/PANGAEA.921576, 2020.

Bialas, J., Klaucke, I., and Haeckel, M.: FS MARIA S. MERIAN Fahrtbericht / Cruise Report MSM34/1 & 2 - SUGAR Site ; Varna – Varna, 06.12.13 – 16.01.14, GEOMAR Helmholtz-Zentrum für Ozeanforschung Kiel, https://doi.org/10.3289/geomar_rep_ns_15_2014, 2014.

Bialas, J., Papenberg, C., and Riedel, M.: 3D P-cable seismic data during Maria S. Merian cruise MSM34, Black Sea, 615 https://doi.org/10.1594/PANGAEA.921631, 2020a.

Bialas, J., Bohlen, T., Dannowski, A., Eisenberg-Klein, G., Gassner, L., Gehrmann, R., Heeschen, K., Hölz, S., Jegen, M., Klaucke, I., Krieger, M., Mann, J., Müller, C., Prüßmann, J., Schicks, J., Schünemann, E., Schwalenberg, K., Sommer, M., Smilde, P. L., Spangenberg, E., Trappe, H., and Zander, T.: Joint interpretation of geophysical field experiments in the danube deep-sea fan, Black Sea, Marine and Petroleum Geology, 104551, https://doi.org/10.1016/j.marpetgeo.2020.104551, 2020b.

620 Bohrmann, G., Ahrlich, F., Bachmann, K., and et al.: Short cruise report R/V Meteor cruise report M142 - Drilling Gas Hydrates in the Danube Deep-Sea Fan, Black Sea, Varna - Varna, 04 November - 09 December 2017, MARUM Universität Bremen, 2018.

Boswell, R., Collett, T. S., Frye, M., Shedd, W., McConnell, D. R., and Shelander, D.: Subsurface gas hydrates in the northern Gulf of Mexico, Marine and Petroleum Geology, 34, 4–30, https://doi.org/10.1016/j.marpetgeo.2011.10.003, 2012.

625 Boswell, R., Shipp, C., Reichel, T., Shelander, D., Saeki, T., Frye, M., Shedd, W., Collett, T. S., and McConnell, D. R.: Prospecting for marine gas hydrate resources, Interpretation, 4, SA13–SA24, https://doi.org/10.1190/INT-2015-0036.1, 2016.

Burwicz-Galerne, E., Haeckel, M., Hensen, C., Samant, R., and Wallmann, K.: The gas hydrate system of the western Black Sea Basin, Marine and Petroleum Geology, 168, 107026, https://doi.org/10.1016/j.marpetgeo.2024.107026, 2024.

Caress, D. W., Thomas, H., Kirkwood, W. J., McEwen, R., Henthorn, R., Clague, D. A., Paull, C. K., and Paduan, J.: High-630 Resolution Multibeam, Sidescan, and Subbottom Surveys Using the MBARI AUV D. Allan B., Marine habitat mapping technology for Alaska, 47–69, https://doi.org/10.4027/mhmta.2008.04, 2008.

Chand, S. and Minshull, T. A.: Seismic constraints on the effects of gas hydrate on sediment physical properties and fluid flow: a review, Geofluids, 3, 275–289, https://doi.org/10.1046/j.1468-8123.2003.00067.x, 2003.

Chatterjee, R., Mukhopadhyay, M., and Paul, S.: Overpressure zone under the Krishna–Godavari offshore basin: geophysical
635   implications for natural hazard in deeper-water drilling, Nat Hazards, 57, 121–132, https://doi.org/10.1007/s11069-010-9659-6, 2011.

Cobbold, P. R., Mourgues, R., and Boyd, K.: Mechanism of thin-skinned detachment in the Amazon Fan: assessing the
importance of fluid overpressure and hydrocarbon generation, Marine and Petroleum Geology, 21, 1013–1025,
https://doi.org/10.1016/j.marpetgeo.2004.05.003, 2004.

640   Collett, T., Riedel, M., Cochran, J. R., Boswell, R., Kumar, P., and Sathe, A. V.: Indian Continental Margin Gas Hydrate
Prospects: Results of the Indian National Gas Hydrate Program (NGHP) Expedition 01, https://doi.org/10.7916/D8-NF9W-CZ91, 2008.

Collett, T. S., Boswell, R., Cochran, J. R., Kumar, P., Lall, M., Mazumdar, A., Ramana, M. V., Ramprasad, T., Riedel, M.,
Sain, K., Sathe, A. V., and Vishwanath, K.: Geologic implications of gas hydrates in the offshore of India: Results of the
645   National   Gas   Hydrate   Program   Expedition   01,   Marine   and   Petroleum   Geology,   58,   3–28,
https://doi.org/10.1016/j.marpetgeo.2014.07.021, 2014.

Collett, T. S., Boswell, R., Waite, W. F., Kumar, P., Roy, S. K., Chopra, K., Singh, S. K., Yamada, Y., Tenma, N., Pohlman,
J., and Zyrianova, M.: India National Gas Hydrate Program Expedition 02 Summary of Scientific Results: Gas hydrate systems
along   the   eastern   continental   margin   of   India,   Marine   and   Petroleum   Geology,   108,   39–142,
650   https://doi.org/10.1016/j.marpetgeo.2019.05.023, 2019.

Crutchley, G. J., Berndt, C., Geiger, S., Klaeschen, D., Papenberg, C., Klaucke, I., Hornbach, M. J., Bangs, N. L. B., and
Maier, C.: Drivers of focused fluid flow and methane seepage at south Hydrate Ridge, offshore Oregon, USA, Geology, 41,
551–554, https://doi.org/10.1130/G34057.1, 2013.

Damuth, J. E. and Olson, H. C.: Latest Quaternary sedimentation in the northern Gulf of Mexico Intraslope Basin Province: I.
655   Sediment facies and depositional processes, Geosphere, 11, 1689–1718, https://doi.org/10.1130/GES01090.1, 2015.

Dannowski, A. and Bialas, J.: Seismic processed data (Ocean Bottom Seismometer working area dataset, profiles p4102 and
p4103) during RV MARIA S. MERIAN cruise MSM34/2, Black Sea., https://doi.org/10.1594/PANGAEA.987011, 2025.

Deuser, W. G.: Evolution of Anoxic Conditions in Black Sea during Holocene, in: The Black Sea - Geology, Chemistry, and
Biology, vol. 20, edited by: Degens, E. T. and Ross, D. A., American Association of Petroleum Geologists, Tulsa, Oklahoma,
660   133–136, 1974.

Dewangan, P., Sriram, G., Mahale, V. P., and Gaddam, V. K.: A recent catastrophic submarine slope failure in the Krishna-
Godavari basin, Bay of Bengal, India, Landslides, 22, 537–550, https://doi.org/10.1007/s10346-024-02359-w, 2025.

Diehl, T.: 3-D Seismic Velocity Models of the Alpine Crust from Local Earthquake Tomography, Dissertation, ETH Zürich,
Zürich, 189 pp., 2008.

665   Digranes, P., Mjelde, R., Kodaira, S., Shimamura, H., Kanazawa, T., Shiobara, H., and Berg, E. W.: A regional shear-wave
velocity model in the central Vøring Basin, N. Norway, using three-component Ocean Bottom Seismographs, Tectonophysics,
293, 157–174, https://doi.org/10.1016/S0040-1951(98)00093-6, 1998.

Flood, R. D., Manley, P. L., Kowsmann, R. O., Appi, C. J., and Pirmez, C.: Seismic Facies and Late Quaternary Growth of
Amazon Submarine Fan, in: Seismic Facies and Sedimentary Processes of Submarine Fans and Turbidite Systems, edited by:
670   Weimer, P. and Link, M. H., Springer New York, New York, NY, 415–433, https://doi.org/10.1007/978-1-4684-8276-8_23,
1991.

Fujie, G.: MODELING, 2008a.

Fujie, G.: PASTEUP, 2008b.

Fujie, G., Kasahara, J., Murase, K., Mochizuki, K., and Kaneda, Y.: Interactive analysis tools for the wide-angle seismic data
for crustal structure study (Technical Report), Exploration Geophysics, 39, 26–33, https://doi.org/10.1071/EG08006, 2008.

Grevemeyer, I. and Villinger, H.: Gas hydrate stability and the assessment of heat flow through continental margins,
Geophysical Journal International, 145, 647–660, https://doi.org/10.1046/j.0956-540x.2001.01404.x, 2001.

Gupta, S., Deusner, C., Burwicz-Galerne, E., and Haeckel, M.: Numerical analysis of the dynamic gas hydrate system and
multiple BSRs in the Danube paleo-delta, Black Sea, Marine Geology, 469, 107221,
https://doi.org/10.1016/j.margeo.2024.107221, 2024.

Haines, S. S., Hart, P. E., Collett, T. S., Shedd, W., Frye, M., Weimer, P., and Boswell, R.: High-resolution seismic
characterization of the gas and gas hydrate system at Green Canyon 955, Gulf of Mexico, USA, Marine and Petroleum
Geology, 82, 220–237, https://doi.org/10.1016/j.marpetgeo.2017.01.029, 2017.

Hamilton, E. L.: Sound velocity gradients in marine sediments, The Journal of the Acoustical Society of America, 65, 909–
922, https://doi.org/10.1121/1.382594, 1979.

Hillman, J. I. T., Klaucke, I., Bialas, J., Feldman, H., Drexler, T., Awwiller, D., Atgin, O., Çifçi, G., and Badhani, S.: Gas
migration pathways and slope failures in the Danube Fan, Black Sea, Marine and Petroleum Geology, 92, 1069–1084,
https://doi.org/10.1016/j.marpetgeo.2018.03.025, 2018.

Iemelianov, V., Ivanik, O., Kukovska, T., Fedoronchuk, N., Shuraiev, I., Petrushenko, E., and Hadiatska, K.: Modeling and
forecast of gas hydrate distribution in the Black Sea: main principles and approaches, Front. Earth Sci., 13, 1518758,
https://doi.org/10.3389/feart.2025.1518758, 2025.

Ivanik, O., Iemelianov, V., Kukovska, T., Fedoronchuk, N., and Hadiatska, K.: Submarine landslides and assessment of slope
stability in gas hydrate zones, Black Sea region, 18th International Conference Monitoring of Geological Processes and
Ecological Condition of the Environment, Kyiv, Ukraine, 1–5, https://doi.org/10.3997/2214-4609.2025510126, 2025.

Jørgensen, B. B., Böttcher, M. E., Lüschen, H., Neretin, L. N., and Volkov, I. I.: Anaerobic methane oxidation and a deep H2S
sink generate isotopically heavy sulfides in Black Sea sediments, Geochimica et Cosmochimica Acta, 68, 2095–2118,
https://doi.org/10.1016/j.gca.2003.07.017, 2004.

Judd, A. G. and Hovland, M.: The evidence of shallow gas in marine sediments, Continental Shelf Research, 12, 1081–1095,
https://doi.org/10.1016/0278-4343(92)90070-Z, 1992.

Judd, A. G. and Hovland, M.: Seabed fluid flow: the impact of geology, biology and the marine environment, Cambridge
University Press, Cambridge ; New York, 475 pp., 2007.

Keller, G. H.: Organic matter and the geotechnical properties of submarine sediments, Geo-Marine Letters, 2, 191–198,
https://doi.org/10.1007/BF02462762, 1982.

Ker, S. and Riboulot, V.: GHASS cruise report, Ifremer, 2015.

705   Ketzer, J. M., Augustin, A., Rodrigues, L. F., Oliveira, R., Praeg, D., Pivel, M. A. G., Dos Reis, A. T., Silva, C., and Leonel, B.: Gas seeps and gas hydrates in the Amazon deep-sea fan, Geo-Mar Lett, 38, 429–438, https://doi.org/10.1007/s00367-018-0546-6, 2018.

Kumar, P., Collett, T. S., Boswell, R., Cochran, J. R., Lall, M., Mazumdar, A., Ramana, M. V., Ramprasad, T., Riedel, M., Sain, K., Sathe, A. V., Vishwanath, K., and Yadav, U. S.: Geologic implications of gas hydrates in the offshore of India:
710   Krishna–Godavari Basin, Mahanadi Basin, Andaman Sea, Kerala–Konkan Basin, Marine and Petroleum Geology, 58, 29–98, https://doi.org/10.1016/j.marpetgeo.2014.07.031, 2014.

Kunath, P., Crutchley, G., Chi, W., Berndt, C., Liu, C., Elger, J., Klaeschen, D., and Bohrmann, G.: Episodic Venting of a Submarine Gas Seep on Geological Time Scales: Formosa Ridge, Northern South China Sea, JGR Solid Earth, 127, e2022JB024668, https://doi.org/10.1029/2022JB024668, 2022.

715   Lee, M. W. and Collett, T. S.: Pore- and fracture-filling gas hydrate reservoirs in the Gulf of Mexico Gas Hydrate Joint Industry Project Leg II Green Canyon 955 H well, Marine and Petroleum Geology, 34, 62–71, https://doi.org/10.1016/j.marpetgeo.2011.08.002, 2012.

Lericolais, G., Bulois, C., Gillet, H., and Guichard, F.: High frequency sea level fluctuations recorded in the Black Sea since the LGM, Global and Planetary Change, 66, 65–75, https://doi.org/10.1016/j.gloplacha.2008.03.010, 2009.

720   Lericolais, G., Bourget, J., Popescu, I., Jermannaud, P., Mulder, T., Jorry, S., and Panin, N.: Late Quaternary deep-sea sedimentation in the western Black Sea: New insights from recent coring and seismic data in the deep basin, Global and Planetary Change, 103, 232–247, https://doi.org/10.1016/j.gloplacha.2012.05.002, 2013.

Løseth, H., Gading, M., and Wensaas, L.: Hydrocarbon leakage interpreted on seismic data, Marine and Petroleum Geology, 26, 1304–1319, https://doi.org/10.1016/j.marpetgeo.2008.09.008, 2009.

725   Madof, A. S., Baumgardner, S. E., Laugier, F. J., and Haataja, J. I.: Interpretation of Gas Hydrate Province Supported by Petrophysical Analyses: Mississippi Fan, Gulf of Mexico, Geophysical Research Letters, 46, 13253–13261, https://doi.org/10.1029/2019GL085217, 2019.

Maercklin, N.: SUPOLAR and SUPOFILT: SU programs for polarization analysis and filtering of three-component data, https://doi.org/10.13140/2.1.1697.7926, 2001.

730   Maslin, M.: Review of the Timing and Causes of the Amazon-Fan Mass Transport and Avulsion Deposits During the latest Pleistocene, in: External Controls on Deep-Water Depositional Systems, 133–144, 2009.

Mitchell, J. K. and Soga, K.: Fundamentals of soil behavior, 3rd ed., John Wiley & Sons, Hoboken, N.J, 577 pp., 2005.

Mulder, T. and Cochonat, P.: Classification of Offshore Mass Movements, SEPM JSR, Vol. 66, https://doi.org/10.1306/D42682AC-2B26-11D7-8648000102C1865D, 1996.

735   Özsoy, E. and Ünlüata, Ü.: Oceanography of the Black Sea: A review of some recent results, Earth-Science Reviews, 42, 231–272, https://doi.org/10.1016/S0012-8252(97)81859-4, 1997.

Popescu, I., Lericolais, G., Panin, N., Wong, H. K., and Droz, L.: Late Quaternary channel avulsions on the Danube deep-sea fan, Black Sea, Marine Geology, 179, 25–37, https://doi.org/10.1016/S0025-3227(01)00197-9, 2001.

Popescu, I., Lericolais, G., Panin, N., Normand, A., Dinu, C., and Le Drezen, E.: The Danube submarine canyon (Black Sea):
740   morphology and sedimentary processes, Marine Geology, 206, 249–265, https://doi.org/10.1016/j.margeo.2004.03.003, 2004.

Popescu, I., De Batist, M., Lericolais, G., Nouzé, H., Poort, J., Panin, N., Versteeg, W., and Gillet, H.: Multiple bottom-simulating reflections in the Black Sea: Potential proxies of past climate conditions, Marine Geology, 227, 163–176, https://doi.org/10.1016/j.margeo.2005.12.006, 2006.

Popescu, I., Lericolais, G., Panin, N., De Batist, M., and Gillet, H.: Seismic expression of gas and gas hydrates across the western Black Sea, Geo-Mar Lett, 27, 173–183, https://doi.org/10.1007/s00367-007-0068-0, 2007.

Praeg, D., Silva, C. G., Reis, A. T. D., Cruz, A., Ketzer, J. M., Migeon, S., and Gorini, C.: Seismic evidence of gas hydrate and seafloor fluid escape on the upper Amazon deep-sea fan, Brazilian equatorial margin, Braz J Geophys, 40, https://doi.org/10.22564/brjg.v40i3.2175, 2022.

Priest, J. A., Rees, E. V. L., and Clayton, C. R. I.: Influence of gas hydrate morphology on the seismic velocities of sands: VELOCITY OF HYDRATE-BEARING SANDS, J. Geophys. Res., 114, https://doi.org/10.1029/2009JB006284, 2009.

Radhakrishna, M., Twinkle, D., Nayak, S., Bastia, R., and Rao, G. S.: Crustal structure and rift architecture across the Krishna–Godavari basin in the central Eastern Continental Margin of India based on analysis of gravity and seismic data, Marine and Petroleum Geology, 37, 129–146, https://doi.org/10.1016/j.marpetgeo.2012.05.005, 2012.

Rao, G. N.: Sedimentation, stratigraphy, and petroleum potential of Krishna-Godavari basin, East Coast of India, Bulletin, 85, 1623–1643, https://doi.org/10.1306/8626CCDF-173B-11D7-8645000102C1865D, 2001.

Riedel, M., Collett, T. S., Kumar, P., Sathe, A. V., and Cook, A.: Seismic imaging of a fractured gas hydrate system in the Krishna–Godavari Basin offshore India, Marine and Petroleum Geology, 27, 1476–1493, https://doi.org/10.1016/j.marpetgeo.2010.06.002, 2010.

Riedel, M., Freudenthal, T., Bergenthal, M., Haeckel, M., Wallmann, K., Spangenberg, E., Bialas, J., and Bohrmann, G.: Physical properties and core-log seismic integration from drilling at the Danube deep-sea fan, Black Sea, Marine and Petroleum Geology, 114, 104192, https://doi.org/10.1016/j.marpetgeo.2019.104192, 2020.

Riedel, M., Hähnel, L., Bialas, J., Bachmann, A. K., Gaide, S., Wintersteller, P., Klaucke, I., and Bohrmann, G.: Controls on Gas Emission Distribution on the Continental Slope of the Western Black Sea, Front. Earth Sci., 8, 601254, https://doi.org/10.3389/feart.2020.601254, 2021.

Ross, D. A. and Degens, E. T.: Recent Sediments of the Black Sea, in: The Black Sea - Geology, Chemistry, and Biology, vol. 20, edited by: Degens, E. T. and Ross, D. A., American Association of Petroleum Geologists, Tulsa, Oklahoma, 183–199, 1974.

Ruppel, C. D. and Kessler, J. D.: The interaction of climate change and methane hydrates, Reviews of Geophysics, 55, 126–168, https://doi.org/10.1002/2016RG000534, 2017.

Ryan, W. B. F., Pitman, W. C., Major, C. O., Shimkus, K., Moskalenko, V., Jones, G. A., Dimitrov, P., Gorür, N., Sakinç, M., and Yüce, H.: An abrupt drowning of the Black Sea shelf, Marine Geology, 138, 119–126, https://doi.org/10.1016/S0025-3227(97)00007-8, 1997.

Sassen, R., Sweet, S. T., DeFreitas, D. A., Morelos, J. A., and Milkov, A. V.: Gas hydrate and crude oil from the Mississippi Fan Foldbelt, downdip Gulf of Mexico Salt Basin: significance to petroleum system, Organic Geochemistry, 32, 999–1008, https://doi.org/10.1016/S0146-6380(01)00064-X, 2001.

Sava, D. and Hardage, B.: Rock-physics Model for Gas-hydrate Systems Associated with Unconsolidated Marine Sediments, in: Natural Gas Hydrates - Energy Resource Potential and Associated Geologic Hazards, vol. 89, edited by: Collett, T., Johnson, A., Knapp, C., and Boswell, R., American Association of Petroleum Geologists, Tulsa, Oklahoma, 505–524, 2009.

780 Schnellmann, M., Anselmetti, F. S., Giardini, D., and Mckenzie, J. A.: 15,000 Years of mass-movement history in Lake Lucerne: Implications for seismic and tsunami hazards, Eclogae geol. Helv., 99, 409–428, https://doi.org/10.1007/s00015-006-1196-7, 2006.

Schwalenberg, K., Gehrmann, R. A. S., Bialas, J., and Rippe, D.: Analysis of marine controlled source electromagnetic data for the assessment of gas hydrates in the Danube deep-sea fan, Black Sea, Marine and Petroleum Geology, 122, 104650, https://doi.org/10.1016/j.marpetgeo.2020.104650, 2020.

785 Sloan, E. D. and Koh, C. A.: Clathrate hydrates of natural gases., CRC Press, Boca Raton, FL, 2008.

Souza, J. M. G., Cruz, A. M., Cubas, N., Rabe, C., Divies, R., Letouzey, J., Praeg, D. B., Granjeon, D., Silva, C. G., Tadeu Dos Reis, A., and Gorini, C.: New insights into gravitational tectonics of the Amazon deep-sea fan: A comparative study of overpressure mechanisms in the Northwest and Southeast compartments, Marine and Petroleum Geology, 182, 107568, https://doi.org/10.1016/j.marpetgeo.2025.107568, 2025.

790 Starostenko, V. I., Rusakov, O. M., Shnyukov, E. F., Kobolev, V. P., and Kutas, R. I.: Methane in the northern Black Sea: characterization of its geomorphological and geological environments, Geological Society, London, Special Publications, 340, 57–75, https://doi.org/10.1144/SP340.5, 2010.

Stockwell, J. W.: The CWP/SU: Seismic Un∗x package, Computers & Geosciences, 25, 415–419, https://doi.org/10.1016/S0098-3004(98)00145-9, 1999.

795 Svitoch, A. A., Selivanov, A. O., and Yanina, T. A.: Paleohydrology of the Black Sea Pleistocene Basins, Water Resources, 27, 594–603, https://doi.org/10.1023/A:1026661801941, 2000.

Twichell, D. C.: A Review of Recent Depositional Processes on the Mississippi Fan, Eastern Gulf of Mexico, in: Gulf of Mexico Origin, Waters and Biota, vol. 3, Harte Research Institute for Gulf of Mexico Studies Series, Sponsored by Harte Research Institute for Gulf of Mexico Studies, Texas A & M University - Corpus Christi, 141–154, 2009.

800 Urlaub, M., Talling, P. J., and Masson, D. G.: Timing and frequency of large submarine landslides: implications for understanding triggers and future geohazard, Quaternary Science Reviews, 72, 63–82, https://doi.org/10.1016/j.quascirev.2013.04.020, 2013.

Vanneste, M., Sultan, N., Garziglia, S., Forsberg, C. F., and L'Heureux, J.-S.: Seafloor instabilities and sediment deformation processes: The need for integrated, multi-disciplinary investigations, Marine Geology, 352, 183–214, 805 https://doi.org/10.1016/j.margeo.2014.01.005, 2014.

Vassilev, A. and Dimitrov, L.: Spatial and Quantity Evaluation of the Black Sea Gas Hydrates, Geologiya i Geofizika, 43, 672–684, 2002.

Weimer, P.: Sequence Stratigraphy, Facies Geometries, and Depositional History of the Mississippi Fan, Gulf of Mexico, Bulletin, 74, 425–453, https://doi.org/10.1306/0C9B2321-1710-11D7-8645000102C1865D, 1990.

810 Wessel, P., Luis, J. F., Uieda, L., Scharroo, R., Wobbe, F., Smith, W. H. F., and Tian, D.: The Generic Mapping Tools Version 6, Geochemistry, Geophysics, Geosystems, 20, 5556–5564, https://doi.org/10.1029/2019GC008515, 2019a.

Wessel, P., Luis, J. F., Uieda, L., Scharroo, R., Wobbe, F., Smith, W. H. F., and Tian, D.: The Generic Mapping Tools version 6, , https://doi.org/10.5281/ZENODO.3407866, 2019b.

Winguth, C.: Pleistozäne Meeresspiegelschwankungen und Sedimentation im nordwestlichen Schwarzen Meer, Dissertation, 815 Institut für Biogeochemie und Meereschemie, Hamburg, 128 pp., 1998.

Winguth, C., Wong, H. K., Panin, N., Dinu, C., Georgescu, P., Ungureanu, G., Krugliakov, V. V., and Podshuveit, V.: Upper Quaternary water level history and sedimentation in the northwestern Black Sea, Marine Geology, 167, 127–146, https://doi.org/10.1016/S0025-3227(00)00024-4, 2000.

Wintersteller, P. and Bialas, J.: Gridded bathymetry from multibeam echosounder EM122 data of the cruise MSM34/2 (2013), 820 https://doi.org/10.1594/PANGAEA.860486, 2016.

Wong, H. K., Winguth, C., Panin, N., Dinu, C., Wollschläger, M., Georgescu, P., Ungureanu, G., Krugliakov, V. V., and Podshuveit, V.: The Danube and Dniepr Fans: Morphostructure and Evolution, GeoEcoMarina, 2, 77–101, 1997.

Yip, Y. H., Jeong, H., Fu, S., and Van Nierop, E. A.: Comparison of CO2 and CH4 Recovery from a Storage Site, Energy Procedia, 37, 4843–4852, https://doi.org/10.1016/j.egypro.2013.06.394, 2013.

825 Yun, T. S., Francisca, F. M., Santamarina, J. C., and Ruppel, C.: Compressional and shear wave velocities in uncemented sediment containing gas hydrate, Geophys. Res. Lett., 32, L10609 (1-5), https://doi.org/10.1029/2005GL022607, 2005.

Zander, T., Haeckel, M., Berndt, C., Chi, W.-C., Klaucke, I., Bialas, J., Klaeschen, D., Koch, S., and Atgın, O.: On the origin of multiple BSRs in the Danube deep-sea fan, Black Sea, Earth and Planetary Science Letters, 462, 15–25, https://doi.org/10.1016/j.epsl.2017.01.006, 2017.

830 Zander, T., Choi, J. C., Vanneste, M., Berndt, C., Dannowski, A., Carlton, B., and Bialas, J.: Potential impacts of gas hydrate exploitation on slope stability in the Danube deep-sea fan, Black Sea, Marine and Petroleum Geology, 92, 1056–1068, https://doi.org/10.1016/j.marpetgeo.2017.08.010, 2018.

Zelt, C. A.: Modelling strategies and model assessment for wide-angle seismic traveltime data, Geophysical Journal International, 139, 183–204, https://doi.org/10.1046/j.1365-246X.1999.00934.x, 1999.

835 Zelt, C. A. and Smith, R. B.: Seismic traveltime inversion for 2-D crustal velocity structure, Geophysical Journal International, 108, 16–34, https://doi.org/10.1111/j.1365-246X.1992.tb00836.x, 1992.